

Unconventional Mixed-Parity Magnetism in Rare-Earth Tetraborides

Dong-Choon Ryu^{1,2,*}, Jae-Ho Han³, Bongjae Kim^{4,†} and Chang-Jong Kang^{1,2‡}

¹*Department of Physics, Chungnam National University, Daejeon 34134, Korea*

²*Institute for Sciences of the Universe, Chungnam National University, Daejeon, 34134, Korea*

³*Department of Physics and Chemistry, Korea Military Academy, Seoul 01805, Korea*

⁴*Department of Physics, Kyungpook National University, Daegu, 41566, Korea*

(Dated: July 3, 2026)

Altermagnetism has advanced the study of compensated magnets by revealing non-relativistic spin splitting, traditionally classified into strictly even- or odd-parity spin textures. Here, we unveil a fundamentally different regime: component-resolved mixed-parity spin splitting in a fully three-dimensional compensated magnet. Using first-principles calculations, tight-binding and $\mathbf{k} \cdot \mathbf{p}$ models, along with spin-group symmetry analysis, we demonstrate that the non-coplanar ground state of TbB_4 enforces a unique momentum-space spin texture. The in-plane spin components exhibit odd-parity p - and f -wave-like textures, whereas the out-of-plane component retains an even-parity d -wave altermagnetic character. Crucially, the coexistence of the in-plane odd-parity textures is driven not by relativistic spin-orbit coupling, but by a staggered Berry phase arising from the inherent scalar spin chirality. This mixed-parity structure dictates distinct transport fingerprints, including bulk non-relativistic Edelstein and spin Hall responses, as well as a symmetry-allowed Berry curvature dipole. These results establish the rare-earth tetraborides as a robust platform for engineering complex spin-charge conversion phenomena.

Introduction – Altermagnetism (AM) has recently emerged as a distinct class of magnetism [1–6], attracting growing research interest as a platform for symmetry-driven spintronics [7–10]. AM combines features of both ferromagnetism (FM) and antiferromagnetism (AFM): it exhibits spin splitting in the electronic structure, as in FM, while retaining the compensated net magnetization characteristic of AFM. This unusual coexistence of spin splitting and compensated magnetism distinguishes AM from conventional magnetic phases. A defining hallmark of AM is the momentum \mathbf{k} -dependent even-parity spin splitting, $\varepsilon(s, \mathbf{k}) = \varepsilon(s, -\mathbf{k})$ (spin $s = \uparrow, \downarrow$), which is typically characterized by d -, g -, or i -wave spin textures. Representative material candidates include RuO_2 [9, 11–15], MnTe [16–21], and CrSb [22–26], all of which feature collinear magnetic orders. Recently, this paradigm has been extended to non-collinear or non-coplanar magnetic orders. For instance, MnTe_2 exhibits an even-parity d -wave spin texture constrained by orthogonal glide-mirror symmetries [27].

Parallel to these even-parity phases, recent developments have further broadened the landscape to include odd-parity compensated magnets [28–34]. In such systems, non-collinear but coplanar magnetic orders drive a distinctive spin splitting satisfying $\varepsilon(s, \mathbf{k}) = \varepsilon(-s, -\mathbf{k})$, which is typically protected by non-symmorphic spin-group symmetries [30, 31, 35–39]. Such odd-parity spin textures are particularly important because they can generate a bulk non-relativistic Edelstein effect, *i.e.*, current-induced spin accumulation without relying on spin-orbit coupling, in contrast to the conventional Rashba-Edelstein mechanism [40–44]. These findings establish odd-parity magnets as a distinct route to efficient spin-charge conversion, complementary to the charge-to-spin responses recently discussed in even-parity AMs [45].

Despite these advances, even- and odd-parity spin textures have mostly been treated as separate symmetry classes. However, a natural bulk material in which these spin textures coexist in symmetry-distinct spin channels—producing experimentally accessible transport fingerprints—remains elusive. This motivates the search for compensated magnets hosting component-resolved mixed-parity spin splitting, where magnetoelectric and spin-transport responses normally associated with separate parity classes can emerge within a single magnetic phase.

Rare-earth tetraborides (RB_4) provide a natural material platform for this, owing to their high-symmetry crystal symmetries and diverse, element-specific magnetic ground states [46–52]. For instance, PrB_4 has a ferromagnetic ground state [53], whereas TmB_4 and ErB_4 have collinear AFM order [47]. GdB_4 adopts a non-collinear but coplanar AFM structure that breaks both inversion (P) and time-reversal (T) symmetries individually, but preserves the combined PT symmetry [46]. Recently, the magnetic structure of TbB_4 has been resolved and appears to be distinct from those of other tetraborides. Originally interpreted as a chiral AFM order that breaks both P and T symmetries [54], it has been more accurately reassigned as a complex non-coplanar AFM state [48]. In this configuration, the magnetic order of TbB_4 is a linear combination ($m\Gamma_1^- \oplus m\Gamma_2^+$) of the two distinct magnetic irreducible representations characteristic of TmB_4 ($m\Gamma_2^+$) and GdB_4 ($m\Gamma_1^-$). Since each component possesses distinct parity and time-reversal characteristics, the superposed magnetic structure in TbB_4 yields a complex symmetry landscape, enabling unconventional mixed-parity magnetism.

To explore this possibility, we combine first-principles calculations with tight-binding and $\mathbf{k} \cdot \mathbf{p}$ models, along

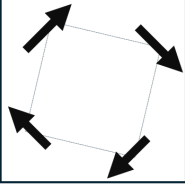
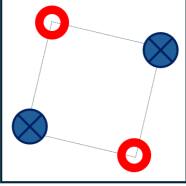
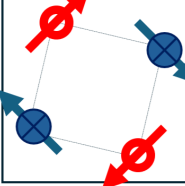
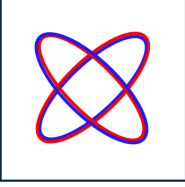
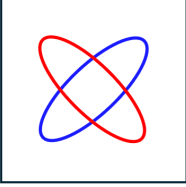
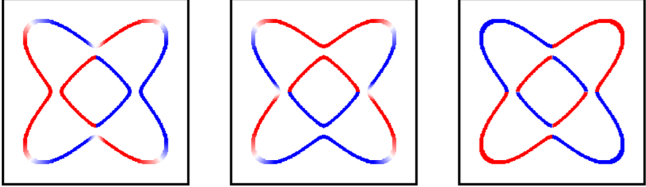
	GdB ₄ ($m\Gamma_1^-$)	TmB ₄ ($m\Gamma_2^+$)	TbB ₄ ($m\Gamma_1^- \oplus m\Gamma_2^+$)
(a) Magnetic structures			
(b) Spin textures	No polarization  PT symmetric	d -wave S_z  $\{C_{2\perp} C_{4z}\}$	odd-parity S_x S_y even-parity S_z  $\{C_{2x} M_y \tau_{0.5a+0.5b}\}, \{C_{2y} M_x \tau_{0.5a+0.5b}\}$
(c) NR Edelstein	$\chi_{ij} = 0$	$\chi_{ij} = 0$	$\chi_{xx}, \chi_{yy} \neq 0, \chi_{zz} = 0$
(d) NR SHE	$\sigma_{xy}^z \neq 0$	$\sigma_{ij}^k = 0$	$\sigma_{xy}^z \neq 0$
(e) BC, BCD	$\Omega_{ij} = 0, D_{ij} = 0$	$\int \Omega_{ij} d\mathbf{k} = 0, D_{ij} = 0$	$\int \Omega_{ij} d\mathbf{k} = 0, D_{xx}, D_{yy} \neq 0$

FIG. 1. (Color Online) Comparative summary of the symmetry-driven phenomena in GdB₄, TmB₄, and TbB₄. (a) Magnetic structures of the three compounds. In GdB₄, the preserved PT symmetry completely suppresses (b) the Fermi surface spin polarization, (c) the non-relativistic Edelstein effect (NREE) tensor χ_{ij} , and (e) the local Berry curvature (BC), but permits a nonzero (d) non-relativistic spin Hall effect (NR SHE, $\sigma_{xy}^z \neq 0$). TmB₄ acts as a prototypical d -wave altermagnet with a robust spin-split Fermi surface; however, its preserved spatial inversion alongside multiple (screw) rotational and (glide) mirror symmetries enforces zero NREE, zero NR SHE, zero net BC, and zero Berry curvature dipole (BCD). In stark contrast, TbB₄ hosts a unique mixture of odd-parity (s_x, s_y) and even-parity (s_z) spin textures dictated by the non-symmorphic spin-group symmetries $\{C_{2x} || M_y | \tau_{(a/2+b/2)}\}$ and $\{C_{2y} || M_x | \tau_{(a/2+b/2)}\}$. Crucially, the broken spatial inversion symmetry in TbB₄ activates a nonzero NREE and BCD for the in-plane diagonal components (xx and yy) as well as a finite NR SHE ($\sigma_{xy}^z \neq 0$), while the $\{E || M_z\}$ and $C_{4z}PT$ symmetries explicitly force the NREE tensor χ_{zz} and BCD D_{zz} to be zero, respectively. Fermi surfaces in (b) are depicted around the M point. See the main text for further details.

with spin-group symmetry analysis, for the rare-earth tetraborides GdB₄, TmB₄, and TbB₄, as summarized in Fig. 1. We show that GdB₄ is a PT -symmetric compensated antiferromagnet with no spin splitting, whereas TmB₄ realizes a d -wave altermagnetic spin texture within the same material family. TbB₄ exhibits a qualitatively different behavior. Although its real-space magnetic structure constitutes a direct superposition of the GdB₄- and TmB₄-type orders, its momentum-space spin texture defies a mere linear combination. Instead, the non-coplanar order enforces a component-resolved mixed-parity spin splitting: the in-plane spin components form odd-parity textures characterized by the coexistence of f -wave-like and p -wave-like patterns, whereas the out-of-plane component retains an even-parity d -wave altermagnetic texture. We further demonstrate that these distinct parity components give rise to complementary transport fingerprints: the odd-parity in-plane texture generates a bulk non-relativistic Edelstein response, whereas the even-parity out-of-plane texture supports an intrinsic

spin Hall response. Finally, we discuss the emergence of the Berry curvature dipole as a direct consequence of the spin-orbit-coupling-induced breakdown of spin-group symmetries in TbB₄. Together, these results establish TbB₄ as a natural material platform for realizing and probing mixed-parity magnetism.

Computational methods – First-principles calculations were performed using the Vienna Ab initio Simulation Package (VASP) implemented with the projector augmented-wave (PAW) pseudo-potential method [55–57]. To properly account for the strong electron correlation and accurately capture the magnetic ground states of the RB_4 systems, we adopt the GGA + U scheme with $U = 6$ eV and $J = 0.75$ eV. Further computational details are provided in Sec. I of the Supplemental Material (SM) [58].

Magnetic structures and spin textures – As illustrated in Fig. 1, GdB₄ and TmB₄ exemplify two representative AFM orders within the RB_4 family. Adopting their established magnetic structures from previous

works [46–48], we evaluate the electronic band structures and spin textures in the absence of spin-orbit coupling (SOC). The resulting decoupling of spin and spatial degrees of freedom enables a classification of the emergent spin textures based on spin-group symmetry. Detailed electronic structures for RB_4 ($R = \text{Gd}, \text{Tm}, \text{Tb}$) are provided in Sec. II of the SM [58].

For GdB_4 , the magnetic moments of the Gd atoms lie within the in-plane, forming a non-collinear coplanar AFM structure described by the $m\Gamma_1^-$ irreducible representation. This order preserves the combined PT symmetry, even though both P and T are individually broken. Consequently, all bands remain at least Kramers spin degeneracy throughout the entire Brillouin zone, thereby producing no spin splitting in the band structure (See the schematic Fermi surface in Fig. 1(b); for further details, see Sec. III of the SM [58]).

For TmB_4 , the magnetic moments of the Tm atoms are collinearly ordered along the c axis, corresponding to the $m\Gamma_2^+$ symmetry. Here, the moments of two diagonally opposite Tm atoms are aligned in the same direction, while the other two are oriented oppositely (see Fig. 1(a)). This magnetic structure preserves inversion symmetry (P) but breaks both the time-reversal (T) and combined PT symmetries. Due to the anisotropic crystal potential of the boron atoms, which is associated with the spin-group symmetry $\{C_{2\perp} || C_{4z}\}$ (where $C_{2\perp}$ is a C_2 rotation about an axis perpendicular to the spin), the spin texture of TmB_4 exhibits d -wave symmetry. Thus, we identify TmB_4 as the first altermagnetic candidate within the RB_4 family.

The magnetic structure of TbB_4 can be viewed as a linear superposition of those of GdB_4 and TmB_4 , characterized by the $m\Gamma_1^- \oplus m\Gamma_2^+$ symmetry [48]. The out-of-plane magnetic moments comprise a collinear AFM order analogous to TmB_4 , whereas the in-plane moments exhibit a non-collinear AFM order resembling GdB_4 . However, the resulting spin texture is not a simple linear combination of the two. In Fig. 2, the first column displays the spin-projected band structures along a \mathbf{k} -path with $k_z = 0$, while the second column provides schematic representations of the spin polarization distribution for each component across the entire Brillouin zone (BZ). Notably, the out-of-plane spin component (s_z) exhibits an even-parity altermagnetic spin texture, whereas the in-plane spin components (s_x and s_y) show odd-parity spin textures. This behavior stands in stark contrast to previous models of odd-parity (p -wave) magnetism, where symmetry constraints strictly forbid in-plane spin polarization while allowing only out-of-plane textures [28, 29].

Now, we conduct a symmetry analysis of TbB_4 (a full list of spin-group symmetry elements is provided in Appendix A). The operations $\{C_{2x} || M_y | \tau_{(a/2+b/2)}\}$ and $\{C_{2y} || M_x | \tau_{(a/2+b/2)}\}$ within the $m\Gamma_1^- \oplus m\Gamma_2^+$ symmetry

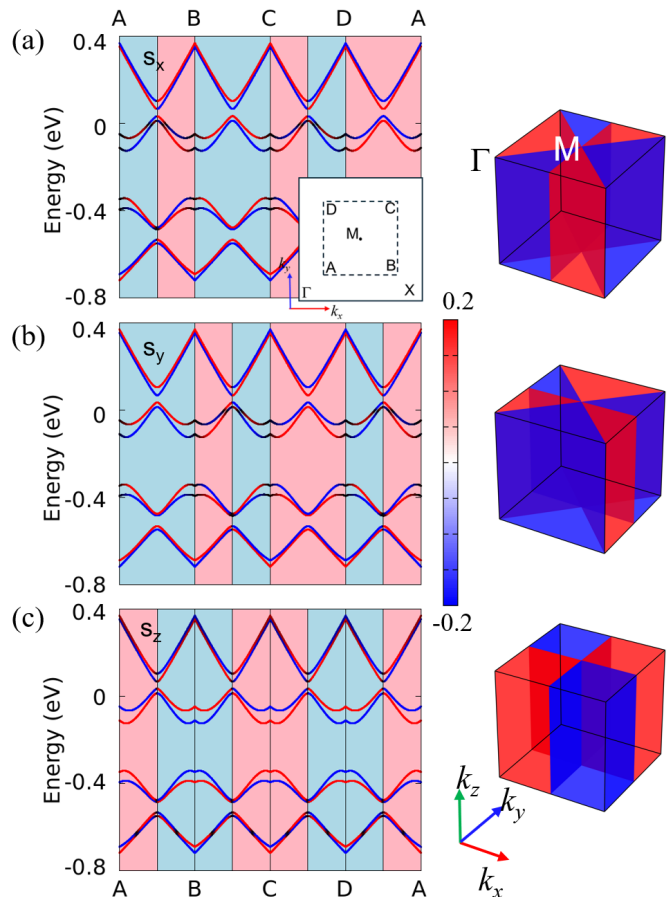


FIG. 2. (Color Online) Component-wise spin splitting in the bulk band structures of TbB_4 . (a)-(c) Spin-projected band structures evaluated at the $k_z = 0$ plane for the s_x , s_y , and s_z components, respectively, with the magnitude of spin polarization indicated by the color bar on the right. The detailed \mathbf{k} -path is illustrated in the inset of (a), where the length ratio of AM to Γ M is set to 0.2. The rightmost panels display schematic representations of the spin polarization distribution for each component across the entire Brillouin zone (BZ). Red and blue colors denote spin-up and spin-down polarizations, respectively.

group yield the following relations in the band dispersion:

$$\begin{aligned} \varepsilon(\mathbf{s}_{\parallel}, \mathbf{k}) &= \varepsilon(-\mathbf{s}_{\parallel}, -\mathbf{k}), \\ \varepsilon(s_z, \mathbf{k}) &= \varepsilon(s_z, -\mathbf{k}), \end{aligned} \quad (1)$$

where $\mathbf{s}_{\parallel} = (s_x, s_y)$ denotes the in-plane spin components (see Appendix B for details). These symmetry-enforced constraints strictly dictate the mixed-parity spin textures in TbB_4 , characterized by odd-parity s_x and s_y components alongside an even-parity s_z component. Furthermore, our tight-binding and $\mathbf{k} \cdot \mathbf{p}$ models (detailed in Appendix C and Secs. IV and V of the SM [58]) reveal that the coexistence of the in-plane p - and f -wave-like spin textures (see Fig. 1(b)) is driven not by spin-orbit coupling, but by an emergent staggered Berry phase induced by scalar spin chirality inherent to TbB_4 . This

gauge field enables the linear momentum terms responsible for the inner p -wave-like pocket, while the lattice geometry dictates the outer f -wave-like modulation.

Thus, in TbB_4 , the out-of-plane spin component exhibits even (d -wave) parity, whereas the in-plane spin components exhibit odd (p - and f -wave-like) parity. These findings establish a novel class of unconventional magnetism, demonstrating a definitive route to stabilizing odd-parity spin textures through a mechanism entirely independent of previously reported p -wave magnetism [28, 29]. Next, we investigate the physical consequences and observable quantities induced by this unique coexistence of even- and odd-parity spin textures in TbB_4 .

Non-relativistic Edelstein effect – The non-relativistic Edelstein effect (NREE) is a key transport fingerprint of odd-parity spin textures, reflecting electric-field-induced spin accumulation without relying on SOC [41–43]. Since TbB_4 hosts odd-parity in-plane spin components, a finite bulk NREE provides a direct probe of the odd-parity sector within its mixed-parity spin texture. To quantify this, we evaluate the Edelstein tensor χ_{ij} , which describes spin accumulation S_i induced by an external electric field E_j via the relation $S_i = \chi_{ij}E_j$ ($i, j \in \{x, y, z\}$). Following linear response theory [42, 59], the total Edelstein tensor can be decomposed into intraband and interband contributions: $\chi = \chi^{\text{intra}} + \chi^{\text{inter}}$, where

$$\chi_{ij}^{\text{intra}} = -\frac{e\hbar}{\pi V N} \sum_{\mathbf{k}, m, n} \frac{\Gamma^2 \text{Re}(\langle n\mathbf{k} | \hat{s}_i | m\mathbf{k} \rangle \langle m\mathbf{k} | \hat{v}_j | n\mathbf{k} \rangle)}{[(E_f - \epsilon_{n\mathbf{k}})^2 + \Gamma^2][(E_f - \epsilon_{m\mathbf{k}})^2 + \Gamma^2]}, \quad (2)$$

$$\chi_{ij}^{\text{inter}} = -\frac{2e\hbar}{\pi V N} \sum_{\mathbf{k}} \sum_{\substack{n \in \text{occ} \\ m \in \text{unocc}}} \frac{\text{Im}(\langle n\mathbf{k} | \hat{s}_i | m\mathbf{k} \rangle \langle m\mathbf{k} | \hat{v}_j | n\mathbf{k} \rangle)}{(\epsilon_{n\mathbf{k}} - \epsilon_{m\mathbf{k}})^2}. \quad (3)$$

Here, Γ represents the phenomenological scattering rate. The terms $|n\mathbf{k}\rangle$ and $\epsilon_{n\mathbf{k}}$ denote the Bloch state and its corresponding energy eigenvalue for the n -th band, with E_f being the Fermi energy. Finally, \hat{s}_i and \hat{v}_j are the i -th component of the spin operator and the j -th component of the velocity operator, respectively.

The spin-group symmetries of TbB_4 strictly restrict the non-zero elements of the Edelstein tensor χ_{ij} . Specifically, the operation $\{E || M_z\}$ enforces the constraint $\chi_{zz}E_z = -\chi_{zz}E_z$, which requires $\chi_{zz} = 0$. The screw-rotation operation $\{C_{2y} || C_{2y} | \tau_{(a/2+b/2)}\}$ imposes $\chi_{yx}E_x = -\chi_{yx}E_x$ and $\chi_{yz}E_z = -\chi_{yz}E_z$, yielding $\chi_{yx} = \chi_{yz} = 0$; similarly, the operation $\{C_{2x} || C_{2x} | \tau_{(a/2+b/2)}\}$ dictates $\chi_{xy} = \chi_{xz} = 0$. Furthermore, the operation $\{I_s C_{4z}^{-1} || C_{4z}\}$ relates the remaining tensor elements, enforcing $\chi_{xx}^{\text{intra}} = -\chi_{yy}^{\text{intra}}$ and $\chi_{xx}^{\text{inter}} = \chi_{yy}^{\text{inter}}$ [60]. Consequently, the only symmetry-allowed components are

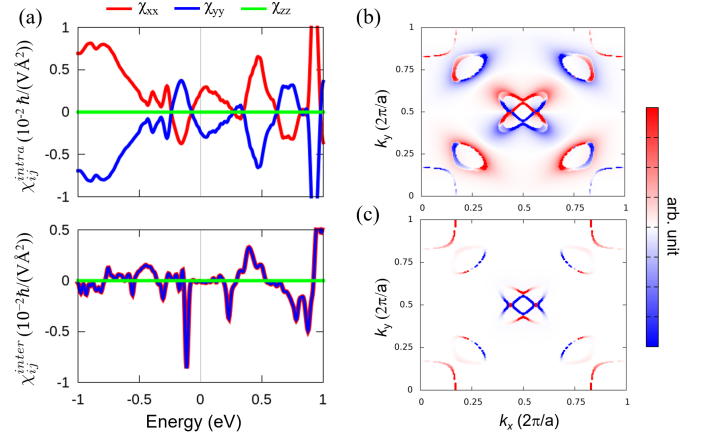


FIG. 3. (Color Online) (a) Non-relativistic Edelstein response tensors χ_{ij}^{intra} (top) and χ_{ij}^{inter} (bottom) calculated with a scattering rate of $\Gamma = 0.01$ eV. Due to the $\{I_s C_{4z}^{-1} || C_{4z}\}$ symmetry, the specific relations $\chi_{xxx}^{\text{intra}} = -\chi_{yyy}^{\text{intra}}$ and $\chi_{xxx}^{\text{inter}} = \chi_{yyy}^{\text{inter}}$ are strictly satisfied. Spin Berry curvatures (b) Ω_{xy}^x and (c) Ω_{xy}^z in the $k_z = 0$ plane, evaluated in the absence of spin-orbit coupling.

χ_{xx} and χ_{yy} . As expected, our first-principles calculations yield finite, non-zero profiles for both χ_{xx} and χ_{yy} . In Fig. 3(a), we plot these components alongside χ_{zz} as functions of the Fermi energy. Note that $\chi_{zz} = 0$ is identically maintained, and the symmetry-enforced relations for the intra- and inter-band contributions are strictly satisfied.

Non-relativistic spin Hall effect – While the non-relativistic Edelstein response probes the odd-parity in-plane sector of TbB_4 , the mixed-parity character of this system also requires a transport signature associated with the even-parity out-of-plane spin texture. The spin-splitter effect (or non-relativistic spin Hall effect) provides such a complementary fingerprint: the even-parity s_z texture can generate a macroscopic spin current without relying on SOC, whereas the odd-parity in-plane contributions cancel upon Brillouin-zone integration by symmetry. The corresponding spin Hall conductivity σ_{jk}^i , which relates the generated spin current J_j^i to the applied electric field E_k via $J_j^i = \sigma_{jk}^i E_k$ (where i and j denote the spin polarization and current propagation directions, respectively), is evaluated using the linear-response Kubo formalism (see Appendix D).

Based on symmetry arguments, the non-relativistic spin Hall effect associated with the odd-parity spin components vanishes; specifically, the $\{C_{2z} || P\}$ symmetry forces all in-plane components to vanish $\sigma_{ij}^x = \sigma_{ij}^y = 0$ (see Appendix D for details). This behavior is analogous to that observed in the odd-parity magnet CeNiAsO [43]. In contrast, the non-relativistic spin Hall conductivity for the even-parity spin component, σ_{xy}^z , is allowed to be non-zero. Although the local spin Berry curvature exhibits non-zero values for both the Ω_{xy}^x and Ω_{xy}^z com-

ponents (Figs. 3(b), (c)), integrating it over the entire Brillouin zone results in an exact cancellation for Ω_{xy}^x while yielding a finite value for Ω_{xy}^z , thereby generating a macroscopic spin Hall conductivity in TbB₄.

Effects of SOC and Berry curvature dipole –

When SOC is taken into account, the symmetry analysis must transition to the magnetic space group framework. The effect of SOC on spin textures of the Fermi surface is discussed in Sec. VI of the SM [58]. For the Edelstein response in TbB₄, only the diagonal components of χ remain, enforced by the three magnetic rotational symmetries: $C_{2x}\tau_{(a/2+b/2)}$, $C_{2y}\tau_{(a/2+b/2)}$, and C_{2z} . For example, the screw-rotation symmetry $C_{2x}\tau_{(a/2+b/2)}$ imposes the constraints $\chi_{xj} = \chi_{jx} = 0$ ($j = y, z$). Moreover, since the spin-group symmetry $\{E||M_z\}$ is absent once SOC is included, χ_{zz} is, in principle, allowed to be nonzero. However, the combined symmetry $C_{4z}PT$ enforces $\chi_{zz}^{\text{intra}} = 0$, whereas the interband component χ_{zz}^{inter} can survive because χ^{inter} corresponds to the imaginary part of the response (see Eq. (3) and Sec. VII of the SM [58] for details).

The emergence of a Berry curvature dipole (BCD) [61], defined as $D_{ij} = \int d\mathbf{k} \sum_n f_{n\mathbf{k}} \partial_{k_i} \Omega_{j,n}(\mathbf{k})$, is the most prominent effect induced by SOC. While the PT symmetry in GdB₄ forces $\Omega_i(\mathbf{k}) = 0$ and the inversion symmetry P in TmB₄ dictates a vanishing BCD, TbB₄ uniquely hosts a finite macroscopic BCD. Without SOC, the spin group operation $\{C_{2z}||P\}$ in TbB₄ acts similarly to P , enforcing an exact momentum-space cancellation of the BCD integral (see Sec. VIII of the SM [58]).

However, SOC fundamentally alters these constraints. Specifically, the magnetic rotational symmetries $C_{2x}\tau_{(a/2+b/2)}$, $C_{2y}\tau_{(a/2+b/2)}$, and C_{2z} restrict D_{ij} to a diagonal form, and the $C_{4z}PT$ symmetry strictly enforces $D_{zz} = 0$ alongside $D_{xx} = -D_{yy}$. Crucially, C_{2z} requires the in-plane Berry curvature to satisfy $\Omega_i(\mathbf{k}_{\parallel}, k_z) = -\Omega_i(-\mathbf{k}_{\parallel}, k_z)$, where $\mathbf{k}_{\parallel} = (k_x, k_y)$. Consequently, their momentum derivatives become even functions with respect to the in-plane momentum \mathbf{k}_{\parallel} . This inherently avoids cancellation during the Brillouin zone integration, yielding a finite BCD, which is robustly corroborated by our calculated Berry curvature under SOC (see Fig. 4).

Concluding Remarks – We have demonstrated that component-resolved mixed-parity spin splitting can be realized in a fully three-dimensional compensated magnet, establishing rare-earth tetraborides as a natural platform for symmetry-engineered spin textures. Within this family, GdB₄ represents a PT -symmetric antiferromagnet in which the combined symmetry enforces spin degeneracy throughout the Brillouin zone. TmB₄, by contrast, hosts a collinear antiferromagnetic order along the c axis and realizes a d -wave altermagnetic spin texture, identifying it as an intrinsic altermagnetic candidate in the RB₄ family. TbB₄ exhibits a qualitatively different regime. Although its non-coplanar magnetic order can be viewed as a combination of the GdB₄- and TmB₄-

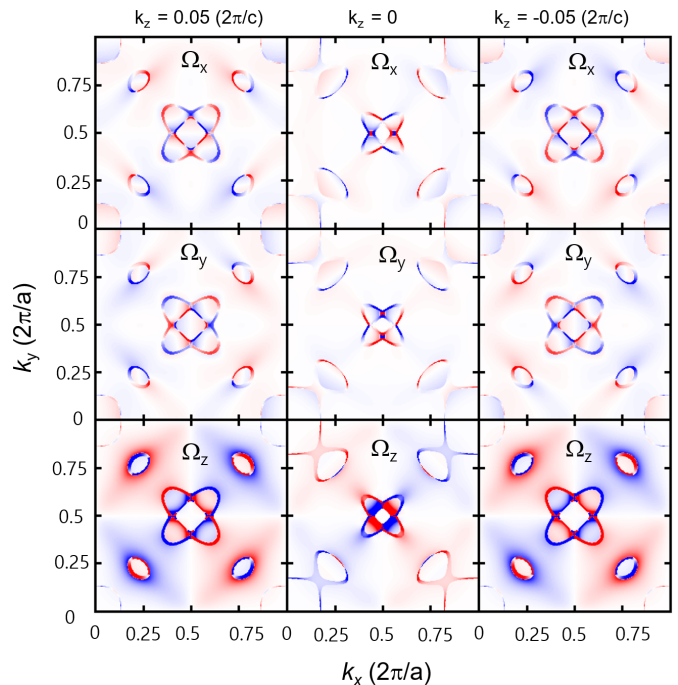


FIG. 4. (Color Online) Momentum-space distribution of the Berry curvature $\Omega_i(\mathbf{k})$ for TbB₄ in the presence of spin-orbit coupling, evaluated on the $k_z = -0.05, 0$, and 0.05 planes (in units of $2\pi/c$).

type magnetic irreducible representations, the resulting momentum-space spin texture is not a simple superposition of the two. Instead, the nonsymmorphic spin-group symmetries of TbB₄ enforce odd-parity p - and f -wave-like textures for the in-plane spin components s_x and s_y , while the out-of-plane component s_z retains an even-parity d -wave altermagnetic character. Crucially, the coexistence of p - and f -wave-like textures originates from a staggered Berry phase induced by the scalar spin chirality inherent to TbB₄, rather than from relativistic spin-orbit coupling.

The coexistence of these mixed-parity sectors leads to distinct transport fingerprints: the odd-parity in-plane texture generates a bulk non-relativistic Edelstein response, whereas the even-parity out-of-plane texture supports a non-relativistic spin Hall response. In the presence of SOC, TbB₄ further develops a symmetry-allowed Berry curvature dipole, providing an additional route to nonlinear Hall phenomena [61]. These results establish TbB₄ as a natural bulk platform for realizing and probing mixed-parity magnetism, and suggest rare-earth tetraborides as a broader materials family for engineering non-relativistic spin-charge conversion in compensated magnets.

Note added.— During the preparation of our manuscript, we became aware of recent theoretical works exploring routes toward mixed-parity spin splitting in collinear spin-orbital magnets and externally tunable al-

termagnetic systems [62, 63]. While these studies provide valuable theoretical frameworks, their proposed mixed-parity states primarily rely on relativistic spin-orbit coupling or external driving fields (such as circularly polarized light). In contrast, our work establishes TbB_4 as a natural bulk material that intrinsically hosts component-resolved mixed-parity magnetism. This unique state emerges purely from the intrinsic non-coplanar magnetic ground state and non-symmorphic constraints, operating entirely independent of spin-orbit coupling or external tuning.

Acknowledgment— We are grateful to Igor Mazin, Hyun-Woo Lee, Yong Baek Kim, Hae-Young Kee, Kyoung-Whan Kim, and Hosub Jin for useful discussions. D.-C. R. and C.-J. K. were supported by the National Research Foundation of Korea (NRF) (Grant No. 2022R1C1C1008200) and the KISTI Supercomputing Center (Project No. KSC-2025-CRE-0461). D.-C. R. was supported by NRF (Grant No. RS-2023-00274550). C.-J. K. was also supported by NRF Grant funded by the Korean Government (MOE). B.K. acknowledges support by NRF Grants (No. RS-2024-00401881, No. RS-2026-25472078, and No. RS-2022-NR068223) and KISTI supercomputing Center (Project No. KSC-2023-CRE-0413). This research was supported by Global - Learning & Academic research institution for Master’s-PhD students, and Postdocs (G-LAMP) Program of NRF grant funded by the Ministry of Education (No. RS-2025-25442707). This research was also supported by “Creation of the quantum information science R&D ecosystem (based on human resources)” through the NRF funded by the Korean government (MSIT; Grant No. RS-2023-00256050). We acknowledge the hospitality of the Aspen Center for Physics during the 2026 Aspen Winter Conference (Altermagnetism and Unconventional Magnetic Orders in Quantum Materials), and of APCTP (Pohang, Korea) during the conference [APCTP-2025-C01], where fruitful discussions greatly benefited this work.

* dcrhyu@postech.ac.kr

† Co-corresponding: bongjae@knu.ac.kr

‡ Co-corresponding: cjkang87@cnu.ac.kr

- [1] L. Šmejkal, R. González-Hernández, T. Jungwirth, and J. Sinova, Crystal time-reversal symmetry breaking and spontaneous hall effect in collinear antiferromagnets, *Science Advances* **6**, eaaz8809 (2020).
- [2] L. Šmejkal, J. Sinova, and T. Jungwirth, Emerging research landscape of altermagnetism, *Phys. Rev. X* **12**, 040501 (2022).
- [3] L. Šmejkal, J. Sinova, and T. Jungwirth, Beyond conventional ferromagnetism and antiferromagnetism: A phase with nonrelativistic spin and crystal rotation symmetry, *Phys. Rev. X* **12**, 031042 (2022).
- [4] L. Šmejkal, A. H. MacDonald, J. Sinova, S. Nakatsuji, and T. Jungwirth, Anomalous hall antiferromagnets, *Nature Reviews Materials* **7**, 482 (2022).

- [5] T. Jungwirth, R. Fernandes, E. Fradkin, A. MacDonald, J. Sinova, and L. Šmejkal, Altermagnetism: An unconventional spin-ordered phase of matter, *Newton* **1**, 10.1016/j.newton.2025.100162 (2025).
- [6] I. Mazin, Editorial: Altermagnetism—a new punch line of fundamental magnetism, *Phys. Rev. X* **12**, 040002 (2022).
- [7] Z. Zhou, X. Cheng, M. Hu, R. Chu, H. Bai, L. Han, J. Liu, F. Pan, and C. Song, Manipulation of the altermagnetic order in CrSb via crystal symmetry, *Nature* **638**, 645 (2025).
- [8] Y. Zhang, H. Bai, J. Dai, L. Han, C. Chen, S. Liang, Y. Cao, Y. Zhang, Q. Wang, W. Zhu, F. Pan, and C. Song, Electrical manipulation of spin splitting torque in altermagnetic RuO_2 , *Nature Communications* **16**, 5646 (2025).
- [9] S. Noh, G.-H. Kim, J. Lee, H. Jung, U. Seo, G. So, J. Lee, S. Lee, M. Park, S. Yang, Y. S. Oh, H. Jin, C. Sohn, and J.-W. Yoo, Tunneling magnetoresistance in altermagnetic RuO_2 -based magnetic tunnel junctions, *Phys. Rev. Lett.* **134**, 246703 (2025).
- [10] C.-T. Liao, Y.-C. Wang, Y.-C. Tien, S.-Y. Huang, and D. Qu, Separation of inverse altermagnetic spin-splitting effect from inverse spin hall effect in RuO_2 , *Phys. Rev. Lett.* **133**, 056701 (2024).
- [11] Z. Feng, X. Zhou, L. Šmejkal, L. Wu, Z. Zhu, H. Guo, R. González-Hernández, X. Wang, H. Yan, P. Qin, X. Zhang, H. Wu, H. Chen, Z. Meng, L. Liu, Z. Xia, J. Sinova, T. Jungwirth, and Z. Liu, An anomalous hall effect in altermagnetic ruthenium dioxide, *Nature Electronics* **5**, 735 (2022).
- [12] O. Fedchenko, J. Minár, A. Akashdeep, S. W. D’Souza, D. Vasilyev, O. Tkach, L. Odenbreit, Q. Nguyen, D. Kutnyakhov, N. Wind, L. Wenthaus, M. Scholz, K. Rossnagel, M. Hoesch, M. Aeschlimann, B. Stadtmüller, M. Kläui, G. Schönhense, T. Jungwirth, A. B. Hellenes, G. Jakob, L. Šmejkal, J. Sinova, and H.-J. Elmers, Observation of time-reversal symmetry breaking in the band structure of altermagnetic RuO_2 , *Science Advances* **10**, eadj4883 (2024).
- [13] R. González-Hernández, L. Šmejkal, K. Výborný, Y. Yahagi, J. Sinova, T. c. v. Jungwirth, and J. Železný, Efficient electrical spin splitter based on nonrelativistic collinear antiferromagnetism, *Phys. Rev. Lett.* **126**, 127701 (2021).
- [14] D.-F. Shao, S.-H. Zhang, M. Li, C.-B. Eom, and E. Y. Tsymbal, Spin-neutral currents for spintronics, *Nature Communications* **12**, 7061 (2021).
- [15] L. Šmejkal, A. B. Hellenes, R. González-Hernández, J. Sinova, and T. Jungwirth, Giant and tunneling magnetoresistance in unconventional collinear antiferromagnets with nonrelativistic spin-momentum coupling, *Phys. Rev. X* **12**, 011028 (2022).
- [16] S. Lee, S. Lee, S. Jung, J. Jung, D. Kim, Y. Lee, B. Seok, J. Kim, B. G. Park, L. Šmejkal, C.-J. Kang, and C. Kim, Broken kramers degeneracy in altermagnetic MnTe, *Phys. Rev. Lett.* **132**, 036702 (2024).
- [17] O. J. Amin, A. Dal Din, E. Golias, Y. Niu, A. Zakharov, S. C. Fromage, C. J. B. Fields, S. L. Heywood, R. B. Cousins, F. Maccherozzi, J. Krempaský, J. H. Dil, D. Kriegner, B. Kiraly, R. P. Champion, A. W. Rushforth, K. W. Edmonds, S. S. Dhesi, L. Šmejkal, T. Jungwirth, and P. Wadley, Nanoscale imaging and control of alter-

- magnetism in MnTe, *Nature* **636**, 348 (2024).
- [18] J. Krempaský, L. Šmejkal, S. W. D'Souza, M. Hajaoui, G. Springholz, K. Uhlířová, F. Alarab, P. C. Constantinou, V. Strocov, D. Usanov, W. R. Pudelho, R. González-Hernández, A. Birk Hellenes, Z. Jansa, H. Reichlová, Z. Šobáň, R. D. Gonzalez Betancourt, P. Wadley, J. Sinova, D. Kriegner, J. Minár, J. H. Dil, and T. Jungwirth, Altermagnetic lifting of Kramers spin degeneracy, *Nature* **626**, 517 (2024).
- [19] T. Osumi, S. Souma, T. Aoyama, K. Yamauchi, A. Honma, K. Nakayama, T. Takahashi, K. Ohgushi, and T. Sato, Observation of a giant band splitting in altermagnetic MnTe, *Phys. Rev. B* **109**, 115102 (2024).
- [20] A. Hariki, A. Dal Din, O. J. Amin, T. Yamaguchi, A. Badura, D. Kriegner, K. W. Edmonds, R. P. Campion, P. Wadley, D. Backes, L. S. I. Veiga, S. S. Dhesi, G. Springholz, L. Šmejkal, K. Výborný, T. Jungwirth, and J. Kuneš, X-ray magnetic circular dichroism in altermagnetic α -MnTe, *Phys. Rev. Lett.* **132**, 176701 (2024).
- [21] D. Takegami, T. Aoyama, T. Okauchi, T. Yamaguchi, S. Tippireddy, S. Agrestini, M. García-Fernández, T. Mizokawa, K. Ohgushi, K.-J. Zhou, J. Chaloupka, J. Kuneš, A. Hariki, and H. Suzuki, Circular dichroism in resonant inelastic x-ray scattering: Probing altermagnetic domains in MnTe, *Phys. Rev. Lett.* **135**, 196502 (2025).
- [22] J. Ding, Z. Jiang, X. Chen, Z. Tao, Z. Liu, T. Li, J. Liu, J. Sun, J. Cheng, J. Liu, Y. Yang, R. Zhang, L. Deng, W. Jing, Y. Huang, Y. Shi, M. Ye, S. Qiao, Y. Wang, Y. Guo, D. Feng, and D. Shen, Large band splitting in g -wave altermagnet CrSb, *Phys. Rev. Lett.* **133**, 206401 (2024).
- [23] S. Reimers, L. Odenbreit, L. Šmejkal, V. N. Strocov, P. Constantinou, A. B. Hellenes, R. Jaeschke Ubierno, W. H. Campos, V. K. Bharadwaj, A. Chakraborty, T. Denneulin, W. Shi, R. E. Dunin-Borkowski, S. Das, M. Kläui, J. Sinova, and M. Jourdan, Direct observation of altermagnetic band splitting in CrSb thin films, *Nature Communications* **15**, 2116 (2024).
- [24] G. Yang, Z. Li, S. Yang, J. Li, H. Zheng, W. Zhu, P. Pan, Y. Xu, S. Cao, W. Zhao, A. Jana, J. Zhang, M. Ye, Y. Song, L.-H. Hu, L. Yang, J. Fujii, I. Vobornik, M. Shi, H. Yuan, Y. Zhang, Y. Xu, and Y. Liu, Three-dimensional mapping of the altermagnetic spin splitting in CrSb, *Nature Communications* **16**, 1442 (2025).
- [25] N. Biniskos, M. dos Santos Dias, S. Agrestini, D. Sviták, K.-J. Zhou, J. Pospíšil, and P. Čermák, Systematic mapping of altermagnetic magnons by resonant inelastic x-ray circular dichroism, *Nature Communications* **16**, 9311 (2025).
- [26] C. Li, M. Hu, Z. Li, Y. Wang, W. Chen, B. Thiagarajan, M. Leandersson, C. Polley, T. Kim, H. Liu, C. Fulga, M. G. Vergniory, O. Janson, O. Tjernberg, and J. van den Brink, Topological weyl altermagnetism in CrSb, *Communications Physics* **8**, 311 (2025).
- [27] Y.-P. Zhu, X. Chen, X.-R. Liu, Y. Liu, P. Liu, H. Zha, G. Qu, C. Hong, J. Li, Z. Jiang, X.-M. Ma, Y.-J. Hao, M.-Y. Zhu, W. Liu, M. Zeng, S. Jayaram, M. Lenger, J. Ding, S. Mo, K. Tanaka, M. Arita, Z. Liu, M. Ye, D. Shen, J. Wrachtrup, Y. Huang, R.-H. He, S. Qiao, Q. Liu, and C. Liu, Observation of plaid-like spin splitting in a noncoplanar antiferromagnet, *Nature* **626**, 523 (2024).
- [28] A. B. Hellenes, T. Jungwirth, R. Jaeschke-Ubierno, A. Chakraborty, J. Sinova, and L. Šmejkal, p -wave magnets (2024), arXiv:2309.01607 [cond-mat.mes-hall].
- [29] B. Brekke, P. Sukhachov, H. G. Giil, A. Brataas, and J. Linder, Minimal models and transport properties of unconventional p -wave magnets, *Phys. Rev. Lett.* **133**, 236703 (2024).
- [30] Q. Song, S. Stavrić, P. Barone, A. Droghetti, D. S. Antonenko, J. W. F. Venderbos, C. A. Occhialini, B. Ilyas, E. Ergeçen, N. Gedik, S.-W. Cheong, R. M. Fernandes, S. Picozzi, and R. Comin, Electrical switching of a p -wave magnet, *Nature* **642**, 64 (2025).
- [31] Z.-Y. Zhuang, D. Zhu, D. Liu, Z. Wu, and Z. Yan, Odd-parity altermagnetism originated from orbital orders (2025), arXiv:2508.18361 [cond-mat.mes-hall].
- [32] R. Yamada, M. T. Birch, P. R. Baral, S. Okumura, R. Nakano, S. Gao, M. Ezawa, T. Nomoto, J. Masell, Y. Ishihara, K. K. Kolincio, I. Belopolski, H. Sagayama, H. Nakao, K. Ohishi, T. Ohhara, R. Kiyonagi, T. Nakajima, Y. Tokura, T.-h. Arima, Y. Motome, M. M. Hirschmann, and M. Hirschberger, A metallic p -wave magnet with commensurate spin helix, *Nature* **646**, 837 (2025).
- [33] D. McNally, p -wave magnetism in a metal, *Nature Materials* **25**, 16 (2026).
- [34] Q. N. Meier, A. Carta, C. Ederer, and A. Cano, Net and compensated altermagnetism from staggered orbital order: Layer-dependent spin splitting in $sr_{n+1}cr_no_{3n+1}$, *Phys. Rev. Lett.* **136**, 116705 (2026).
- [35] Y. Yu, M. B. Lyngby, T. Shishidou, M. Roig, A. Kreisler, M. Weinert, B. M. Andersen, and D. F. Agterberg, Odd-parity magnetism driven by antiferromagnetic exchange, *Phys. Rev. Lett.* **135**, 046701 (2025).
- [36] P. Liu, J. Li, J. Han, X. Wan, and Q. Liu, Spin-group symmetry in magnetic materials with negligible spin-orbit coupling, *Phys. Rev. X* **12**, 021016 (2022).
- [37] Z. Xiao, J. Zhao, Y. Li, R. Shindou, and Z.-D. Song, Spin space groups: Full classification and applications, *Phys. Rev. X* **14**, 031037 (2024).
- [38] X. Chen, J. Ren, Y. Zhu, Y. Yu, A. Zhang, P. Liu, J. Li, Y. Liu, C. Li, and Q. Liu, Enumeration and representation theory of spin space groups, *Phys. Rev. X* **14**, 031038 (2024).
- [39] Y. Jiang, Z. Song, T. Zhu, Z. Fang, H. Weng, Z.-X. Liu, J. Yang, and C. Fang, Enumeration of spin-space groups: Toward a complete description of symmetries of magnetic orders, *Phys. Rev. X* **14**, 031039 (2024).
- [40] N. A. A. Pari, R. Jaeschke-Ubierno, A. Chakraborty, L. Šmejkal, and J. Sinova, Nonrelativistic linear edelstein effect in helical EuIn_2As_2 , *Phys. Rev. B* **112**, 024404 (2025).
- [41] R. González-Hernández, P. Ritzinger, K. Výborný, J. Železný, and A. Manchon, Non-relativistic torque and edelstein effect in non-collinear magnets, *Nature Communications* **15**, 7663 (2024).
- [42] M. Hu, O. Janson, C. Felser, P. McClarty, J. van den Brink, and M. G. Vergniory, Spin hall and edelstein effects in chiral non-collinear altermagnets, *Nature Communications* **16**, 8529 (2025).
- [43] A. Chakraborty, A. Birk Hellenes, R. Jaeschke-Ubierno, T. Jungwirth, L. Šmejkal, and J. Sinova, Highly efficient non-relativistic edelstein effect in nodal p -wave magnets, *Nature Communications* **16**, 7270 (2025).
- [44] R. R. Neumann, R. Jaeschke-Ubierno, R. Zarzuela, L. Šmejkal, J. Sinova, and A. Mook, Odd-parity-wave magnons and nonrelativistic thermal edelstein effect

- (2026), arXiv:2603.05415.
- [45] J. Lai, T. Yu, P. Liu, L. Liu, G. Xing, X.-Q. Chen, and Y. Sun, *d*-wave flat fermi surface in altermagnets enables maximum charge-to-spin conversion, *Phys. Rev. Lett.* **135**, 256702 (2025).
- [46] J. A. Blanco, P. J. Brown, A. Stunault, K. Katsumata, F. Iga, and S. Michimura, Magnetic structure of Gdb₄ from spherical neutron polarimetry, *Phys. Rev. B* **73**, 212411 (2006).
- [47] L. Ye, T. Suzuki, and J. G. Checkelsky, Electronic transport on the shastry-sutherland lattice in ising-type rare-earth tetraborides, *Phys. Rev. B* **95**, 174405 (2017).
- [48] R. D. Johnson and S. W. Lovesey, Magnetic symmetries of terbium tetraboride (Tbb₄) revealed by resonant x-ray bragg diffraction, *Phys. Rev. B* **110**, 104405 (2024).
- [49] H. Sim, S. Lee, K.-P. Hong, J. Jeong, J. R. Zhang, T. Kamiyama, D. T. Adroja, C. A. Murray, S. P. Thompson, F. Iga, S. Ji, D. Khomskii, and J.-G. Park, Spontaneous structural distortion of the metallic shastry-sutherland system Dyb₄ by quadrupole-spin-lattice coupling, *Phys. Rev. B* **94**, 195128 (2016).
- [50] J. Etourneau, J. Mercurio, A. Berrada, P. Hagenmuller, R. Georges, R. Bourezg, and J. Gianduzzo, The magnetic and electrical properties of some rare earth tetraborides, *Journal of the Less Common Metals* **67**, 531 (1979).
- [51] K. H. J. Buschow and J. H. N. Creyghton, Magnetic properties of rare earth tetraborides, *The Journal of Chemical Physics* **57**, 3910 (1972).
- [52] H. C. Choi, A. Laref, J. H. Shim, S. K. Kwon, and B. I. Min, Electronic structures and magnetic properties of rb₄ (r=yb,pr,gd,tb,dy), *Journal of Applied Physics* **105**, 07E107 (2009).
- [53] G. A. Wigger, E. Felder, R. Monnier, H. R. Ott, L. Pham, and Z. Fisk, Low-temperature phase transitions in the induced-moment system Prb₄, *Phys. Rev. B* **72**, 014419 (2005).
- [54] R. Misawa, K. Arakawa, T. Yoshioka, H. Ueda, F. Iga, K. Tamasaku, Y. Tanaka, and T. Kimura, Resonant x-ray diffraction study using circularly polarized x rays on antiferromagnetic tbb₄, *Phys. Rev. B* **108**, 134433 (2023).
- [55] G. Kresse and J. Furthmüller, Efficient iterative schemes for ab initio total-energy calculations using a plane-wave basis set, *Phys. Rev. B* **54**, 11169 (1996).
- [56] J. P. Perdew, K. Burke, and M. Ernzerhof, Generalized gradient approximation made simple, *Phys. Rev. Lett.* **77**, 3865 (1996).
- [57] G. Kresse and D. Joubert, From ultrasoft pseudopotentials to the projector augmented-wave method, *Phys. Rev. B* **59**, 1758 (1999).
- [58] See Supplemental Material for further computational details, the electronic structures of RB₄, spin textures on the Fermi surfaces, tight-binding and $\mathbf{k}\cdot\mathbf{p}$ models, the effect of spin-orbit coupling on the spin textures and Edelstein response, as well as the Berry curvature and Berry curvature dipole in the absence of spin-orbit coupling. The Supplemental Material includes Refs. [48, 55? -57].
- [59] H. Li, H. Gao, L. P. Zârbo, K. Výborný, X. Wang, I. Garate, F. Doğan, A. Čejchan, J. Sinova, T. Jungwirth, and A. Manchon, Intraband and interband spin-orbit torques in noncentrosymmetric ferromagnets, *Phys. Rev. B* **91**, 134402 (2015).
- [60] The spin-only inversion I_s is forced to become anti-unitary (incorporating the complex conjugation operator \mathcal{K}) in order to preserve the spin commutation relations

when evaluated as a quantum operator in the Kubo formula. Hence, the symmetry operation $\{I_s C_{4z}^{-1} || C_{4z}\}$ becomes $\{I_s C_{4z}^{-1} || \mathcal{K} C_{4z}\} \equiv T \{C_{4z}^{-1} || C_{4z}\}$, where T is the time-reversal operation.

- [61] I. Sodemann and L. Fu, Quantum nonlinear hall effect induced by berry curvature dipole in time-reversal invariant materials, *Phys. Rev. Lett.* **115**, 216806 (2015).
- [62] Z.-Y. Zhuang, J.-X. Hu, S.-B. Zhang, L.-H. Hu, and Z. Yan, Mixed-parity altermagnetism in collinear spin-orbital magnets (2026), arXiv:2605.05205.
- [63] Y. Yu, Tunable odd-parity spin splittings in altermagnets (2026), arXiv:2605.03026.
- [64] G. Y. Guo, S. Murakami, T.-W. Chen, and N. Nagaosa, Intrinsic spin hall effect in platinum: First-principles calculations, *Phys. Rev. Lett.* **100**, 096401 (2008).

END MATTER

Appendix A: Spin-Space Group Symmetry Elements in TbB₄— Based on the spin-space group (SSG) analysis, the non-coplanar magnetic ground state of TbB₄ comprises 16 symmetry operations. These elements are expressed using the generalized Seitz notation $\{R_s || R_r | \mathbf{t}\}$, incorporating Schoenflies crystallographic symbols:

$$\begin{aligned} & \{E || E | \tau_{(0,0,0)}\}, \quad \{E || M_z | \tau_{(0,0,0)}\}, \\ & \{C_{2z} || C_{2z} | \tau_{(0,0,0)}\}, \quad \{C_{2z} || P | \tau_{(0,0,0)}\}, \\ & \{C_{2x} || M_y | \tau_{(a/2+b/2)}\}, \quad \{C_{2x} || C_{2x} | \tau_{(a/2+b/2)}\}, \\ & \{C_{2y} || M_x | \tau_{(a/2+b/2)}\}, \quad \{C_{2y} || C_{2y} | \tau_{(a/2+b/2)}\}, \\ & \{I_s C_{2(1\bar{1}0)} || M_{110} | \tau_{(a/2+b/2)}\}, \quad \{I_s C_{2(1\bar{1}0)} || C_{2(110)} | \tau_{(a/2+b/2)}\}, \\ & \{I_s C_{2(110)} || M_{1\bar{1}0} | \tau_{(a/2+b/2)}\}, \quad \{I_s C_{2(110)} || C_{2(1\bar{1}0)} | \tau_{(a/2+b/2)}\}, \\ & \{I_s C_{4z} || C_{4z}^{-1} | \tau_{(0,0,0)}\}, \quad \{I_s C_{4z} || S_{4z}^{-1} | \tau_{(0,0,0)}\}, \\ & \{I_s C_{4z}^{-1} || C_{4z} | \tau_{(0,0,0)}\}, \quad \{I_s C_{4z}^{-1} || S_{4z} | \tau_{(0,0,0)}\}. \end{aligned}$$

In this notation, R_s acts exclusively on the spin space, R_r acts on the real-space atomic coordinates, and \mathbf{t} denotes the fractional translation vector (e.g., $\tau_{(a/2+b/2)}$ indicates an in-plane translation by half a lattice parameter along both the a and b axes). The symmetry operations (R_s and R_r) are denoted using the Schoenflies nomenclature:

- E and P : The identity and spatial inversion operations, respectively.
- C_n : An n -fold proper rotation.
- M : A mirror reflection across a plane.
- S_4 : A 4-fold improper rotation (roto-reflection).
- I_s : Spin-only inversion.

The subscripts specify the Cartesian or crystallographic direction of the rotation axis or the normal to the mirror plane. The superscript -1 denotes the inverse of the operation (e.g., C_{4z}^{-1} represents a -90° rotation).

Appendix B: Symmetry analysis for mixed-parity spin splitting and spin degeneracy in TbB₄— The non-symmorphic spin group symmetry elements $\{C_{2x}||M_y|\tau_{(a/2+b/2)}\}$ and $\{C_{2y}||M_x|\tau_{(a/2+b/2)}\}$ impose the following constraints on the spin- and momentum-dependent band dispersion $\varepsilon(\mathbf{s}, \mathbf{k})$, respectively:

$$\varepsilon(s_x, s_y, s_z, k_x, k_y, k_z) = \varepsilon(s_x, -s_y, -s_z, k_x, -k_y, k_z), \quad (4)$$

$$\varepsilon(s_x, s_y, s_z, k_x, k_y, k_z) = \varepsilon(-s_x, s_y, -s_z, -k_x, k_y, k_z). \quad (5)$$

Combining these two relations yields:

$$\varepsilon(s_x, s_y, s_z, k_x, k_y, k_z) = \varepsilon(-s_x, -s_y, s_z, -k_x, -k_y, k_z).$$

On each fixed k_z plane, the above relation reduces to:

$$\begin{aligned} \varepsilon(\mathbf{s}_{\parallel}, \mathbf{k}_{\parallel}) &= \varepsilon(-\mathbf{s}_{\parallel}, -\mathbf{k}_{\parallel}), \\ \varepsilon(s_z, \mathbf{k}_{\parallel}) &= \varepsilon(s_z, -\mathbf{k}_{\parallel}), \end{aligned} \quad (6)$$

where $\mathbf{s}_{\parallel} = (s_x, s_y)$ and $\mathbf{k}_{\parallel} = (k_x, k_y)$. Finally, incorporating the spin-group symmetry $\{E||M_z\}$ generalizes these constraints to the full 3D momentum space:

$$\begin{aligned} \varepsilon(\mathbf{s}_{\parallel}, \mathbf{k}) &= \varepsilon(-\mathbf{s}_{\parallel}, -\mathbf{k}), \\ \varepsilon(s_z, \mathbf{k}) &= \varepsilon(s_z, -\mathbf{k}). \end{aligned} \quad (7)$$

These symmetry-enforced constraints robustly explain the mixed-parity spin textures in TbB₄, which are characterized by odd-parity s_x and s_y components alongside an even-parity s_z component.

Furthermore, when $k_x = 0$ or π/a (where $-k_x \equiv k_x$), Eq. (5) simplifies to $\varepsilon(s_x, s_y, s_z, \mathbf{k}) = \varepsilon(-s_x, s_y, -s_z, \mathbf{k})$. This indicates that states with opposite s_x and s_z spin components share the same energy dispersion, thereby enforcing the exact spin degeneracy (i.e., vanishing spin polarization) of s_x and s_z on the $k_x = 0$ and π/a planes. In the same manner, when $k_y = 0$ or π/a , Eq. (4) dictates that $\varepsilon(s_x, s_y, s_z, \mathbf{k}) = \varepsilon(s_x, -s_y, -s_z, \mathbf{k})$, resulting in the spin degeneracy of s_y and s_z on the $k_y = 0$ and π/a planes.

Appendix C: Effective $\mathbf{k} \cdot \mathbf{p}$ Hamiltonian and momentum-dependent spin textures near the M point— To elucidate the microscopic origin of the coexistence of p - and f -wave-like spin textures in the in-plane spin components and the d -wave texture in the out-of-plane spin component, we construct an effective $\mathbf{k} \cdot \mathbf{p}$ Hamiltonian around the M point [$\mathbf{k} = (\pi/a, \pi/a, 0)$]. Let $\mathbf{q} = (q_x, q_y, 0)$ be the small momentum deviation from the M point. The generic effective Hamiltonian is expressed as $\mathcal{H}_{\text{eff}}(\mathbf{q}) = \varepsilon_0(\mathbf{q})\sigma_0 + \mathbf{h}(\mathbf{q}) \cdot \boldsymbol{\sigma}$, where σ_0 is the 2×2 identity matrix, $\boldsymbol{\sigma}$ are the Pauli matrices, and $\mathbf{h}(\mathbf{q})$ is the effective spin-splitting field.

The non-symmorphic spin-group symmetries $\{C_{2x}||M_y|\tau_{(a/2+b/2)}\}$ and $\{C_{2y}||M_x|\tau_{(a/2+b/2)}\}$ strictly

constrain the components of $\mathbf{h}(\mathbf{q})$ up to the third order in \mathbf{q} as follows:

$$\begin{aligned} h_x(\mathbf{q}) &= \alpha_1 q_x + \beta_1 q_x^3 + \gamma_1 q_x q_y^2, \\ h_y(\mathbf{q}) &= \alpha_2 q_y + \beta_2 q_y^3 + \gamma_2 q_x^2 q_y, \\ h_z(\mathbf{q}) &= \lambda q_x q_y, \end{aligned} \quad (8)$$

where $\alpha_1, \alpha_2, \beta_1, \beta_2, \gamma_1, \gamma_2$, and λ are constant coefficients. The resulting energy dispersion of the spin-split bands is given by $\varepsilon_{\pm}(\mathbf{q}) = \varepsilon_0(\mathbf{q}) \pm \sqrt{h_x^2 + h_y^2 + h_z^2}$, and the corresponding spin expectation values are $\langle s_i \rangle_{\pm} = \pm h_i(\mathbf{q})/|\mathbf{h}(\mathbf{q})|$.

This polynomial expansion rigorously demonstrates the momentum-magnitude ($|\mathbf{q}|$) dependent evolution of the in-plane spin textures. For small $|\mathbf{q}|$ (corresponding to the inner Fermi surface), the linear terms dominate over the cubic terms ($|\mathbf{q}| \gg |\mathbf{q}|^3$). Consequently, the in-plane components reduce to $h_x \approx \alpha_1 q_x$ and $h_y \approx \alpha_2 q_y$, yielding a pure p -wave-like spin texture.

Conversely, for larger $|\mathbf{q}|$ (corresponding to the outer Fermi surface), the cubic terms grow rapidly and dominate the spin-splitting field. The in-plane components are then governed by the higher-order harmonics, $h_x \approx q_x(\beta_1 q_x^2 + \gamma_1 q_y^2)$ and $h_y \approx q_y(\beta_2 q_y^2 + \gamma_2 q_x^2)$, which directly manifest as f -wave-like spin textures. Meanwhile, the out-of-plane component h_z is uniquely dictated by the quadratic term $\lambda q_x q_y$, robustly preserving its even-parity d -wave symmetry across the entire momentum space.

Appendix D: Spin Hall Conductivity and spin group symmetry— The spin Hall conductivity σ_{jk}^i is evaluated within the linear response regime using the Kubo formula [64]:

$$\begin{aligned} \sigma_{jk}^i &= -\frac{e}{\hbar} \sum_{\mathbf{k}} \Omega_{jk}^i(\mathbf{k}) = -\frac{e}{\hbar} \sum_{\mathbf{k}} \sum_n f_{n\mathbf{k}} \Omega_{jk,n}^i(\mathbf{k}), \\ \Omega_{jk,n}^i(\mathbf{k}) &= \sum_{m \neq n} \frac{\text{Im}(\langle n\mathbf{k} | \frac{1}{2} \{\hat{s}_i, \hat{v}_j\} | m\mathbf{k} \rangle \langle m\mathbf{k} | \hat{v}_k | n\mathbf{k} \rangle)}{(\epsilon_{n\mathbf{k}} - \epsilon_{m\mathbf{k}})^2}. \end{aligned} \quad (9)$$

Here, e is the electron charge, \hbar is the reduced Planck constant, and $f_{n\mathbf{k}}$ is the Fermi-Dirac distribution function. The terms $|n\mathbf{k}\rangle$ and $\epsilon_{n\mathbf{k}}$ denote the Bloch state and its corresponding energy eigenvalue for the n -th band, respectively. The operators \hat{v} and \hat{s}_i correspond to the velocity and the i -th component of the spin operator, where their anticommutator $\frac{1}{2} \{\hat{s}_i, \hat{v}_j\}$ defines the spin current operator. As shown in Eq. (9), the spin Berry curvature $\Omega_{jk}^i(\mathbf{k})$ is directly proportional to the matrix elements $\langle \{\hat{s}_i, \hat{v}_j\} \hat{v}_k \rangle$. Due to the $\{C_{2z}||P\}$ symmetry (which is common to GdB₄, TmB₄, and TbB₄), the following relations hold: $v_i(\mathbf{k}) = -v_i(-\mathbf{k})$, $s_{x,y}(\mathbf{k}) = -s_{x,y}(-\mathbf{k})$, and $s_z(\mathbf{k}) = s_z(-\mathbf{k})$. Therefore, strict constraints are imposed on the spin Berry curvature: $\Omega_{ij}^{x,y}(\mathbf{k}) = -\Omega_{ij}^{x,y}(-\mathbf{k})$ and $\Omega_{ij}^z(\mathbf{k}) = \Omega_{ij}^z(-\mathbf{k})$. Consequently, all in-plane components of the spin Hall conductivity vanish ($\sigma_{ij}^x = \sigma_{ij}^y =$

0). The $\{E||M_z\}$ symmetry (also shared by all three compounds) further enforces $\sigma_{zx}^z = \sigma_{xz}^z = \sigma_{zy}^z = \sigma_{yz}^z = 0$. Hence, the out-of-plane component σ_{xy}^z remain finite for GdB_4 and TbB_4 . Conversely, in TmB_4 , the spin-group symmetry $\{I_s||C_{2x}|\tau_{(a/2+b/2)}\}$ enforces $\sigma_{xy}^z = \sigma_{yx}^z = 0$, making all components of the spin Hall conductivity vanish.

Supplemental Material for “Unconventional Mixed-Parity Magnetism in Rare-Earth Tetraborides”

Dong-Choon Ryu^{1,2,*} Jae-Ho Han³, Bongjae Kim^{4,†} and Chang-Jong Kang^{1,2‡}

¹Department of Physics, Chungnam National University, Daejeon 34134, Korea

²Institute for Sciences of the Universe, Chungnam National University, Daejeon, 34134, Korea

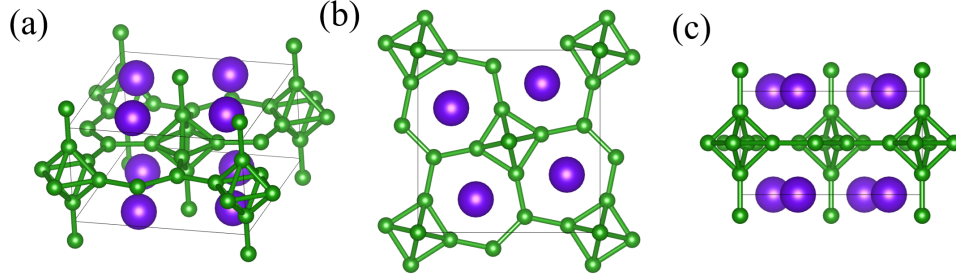
³Department of Physics and Chemistry, Korea Military Academy, Seoul 01805, Korea

⁴Department of Physics, Kyungpook National University, Daegu, 41566, Korea

(Dated: June 25, 2026)

I. CRYSTAL STRUCTURE AND COMPUTATIONAL DETAILS

The rare-earth tetraboride RB_4 crystallizes in a tetragonal structure with the nonsymmorphic $P4/mbm$ space group (SG 127). The crystal structure of RB_4 is illustrated in SFIG. 1. We adopted the experimental lattice constants of $a = 7.119 \text{ \AA}$ and $c = 4.031 \text{ \AA}$ [1]. For the first-principles density functional theory (DFT) calculations, we employed the projector augmented-wave (PAW) method as implemented in the Vienna Ab initio Simulation Package (VASP) within the generalized gradient approximation (GGA) [2–4]. To accurately describe the strongly correlated $4f$ electrons of the Tb atoms, we performed GGA+ U calculations. By varying the on-site Coulomb (U) and exchange (J) parameters, we compared the total energies of various magnetic configurations. The computed total energies are summarized in TABLE I. As shown in TABLE I, the $\Gamma_1^- \oplus \Gamma_2^+$ magnetic configuration is the ground state for $U \geq 6 \text{ eV}$, which is consistent with the experimental result [5].



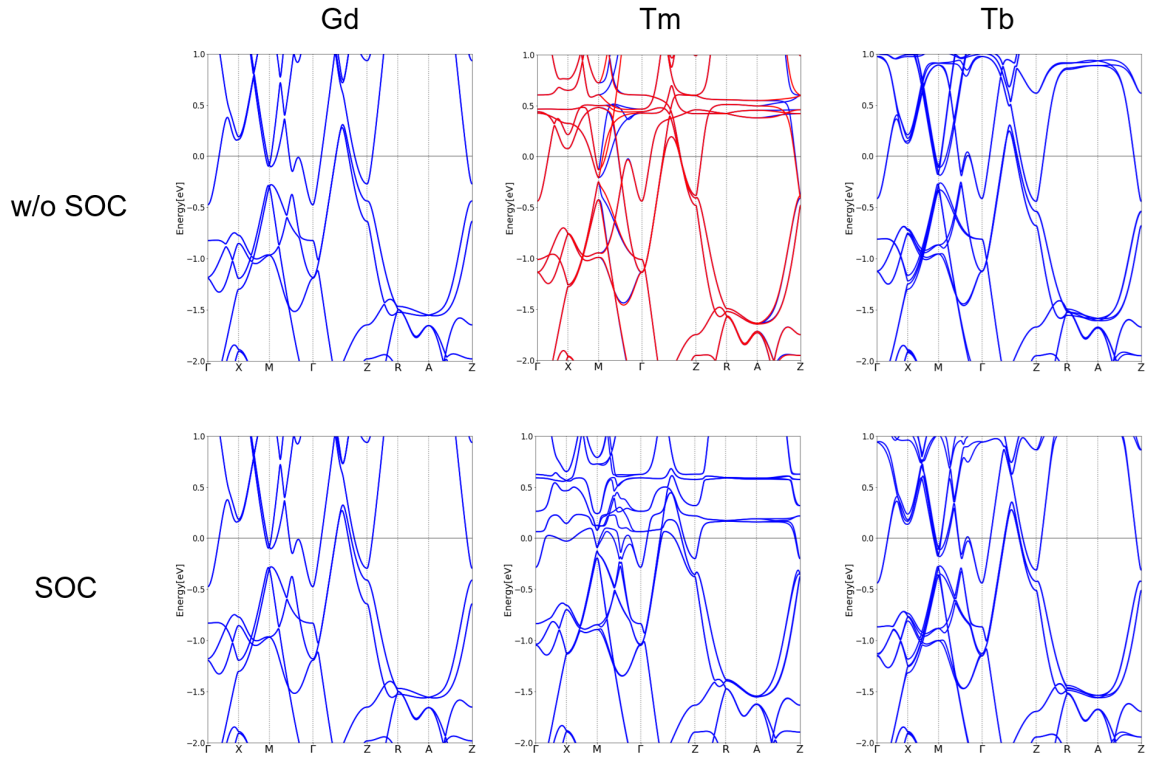
SFIG. 1. (Color Online) Crystal structure of rare-earth tetraborides (RB_4). The large purple and green spheres represent the rare-earth (R) and boron (B) atoms, respectively. (a) Perspective view, (b) top view, and (c) side view.

II. BULK BAND STRUCTURES AND SPIN TEXTURES OF RB_4

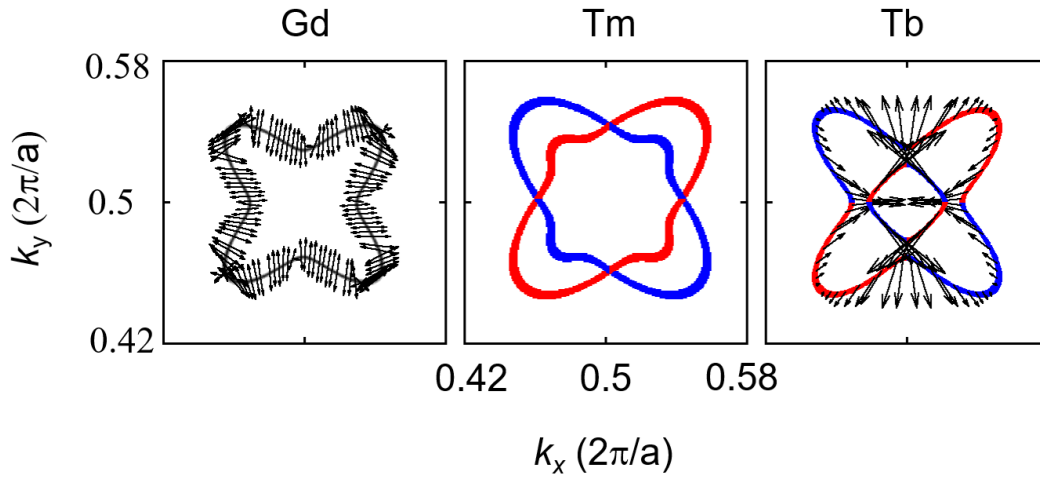
The bulk band dispersions of GdB_4 , TmB_4 , and TbB_4 , calculated both without and with spin-orbit coupling (SOC), are presented in SFIG. 2. GdB_4 exhibits double band degeneracy at all \mathbf{k} -points in the Brillouin zone due to PT symmetry. For TmB_4 , which hosts collinear magnetism, the spin-up and spin-down bands are distinguished by red and blue colors, respectively, in the calculations without SOC. Spin splitting is clearly observed along the Γ – M and Z – A directions, thereby confirming the altermagnetic nature of TmB_4 . The spin textures of GdB_4 , TmB_4 , and TbB_4 are illustrated in SFIG. 3 in the absence of SOC.

TABLE I. Total energy differences per unit cell of TbB_4 for different magnetic structures. Energies are given relative to the $\Gamma_1^- \oplus \Gamma_2^+$ state, which is set to be zero.

	$\Gamma_1^- \oplus \Gamma_2^+$	$\Gamma_2^- \oplus \Gamma_2^+$	$\Gamma_3^- \oplus \Gamma_2^+$	$\Gamma_4^- \oplus \Gamma_2^+$
$U = 4 \text{ eV}, J = 0.5 \text{ eV}$	0	15.89	15.45	-0.34
$U = 6 \text{ eV}, J = 0.75 \text{ eV}$	0	11.91	11.75	0.01
$U = 8 \text{ eV}, J = 1 \text{ eV}$	0	4.376	4.25	0.78



SFIG. 2. (Color Online) Bulk band dispersions of GdB_4 , TmB_4 , and TbB_4 , calculated both without and with SOC. For TmB_4 in the absence of SOC, the spin-up and spin-down bands are depicted in red and blue, respectively, to clearly demonstrate the altermagnetic spin splitting.



SFIG. 3. (Color Online) Spin textures on the Fermi surfaces around the M point for GdB_4 , TmB_4 , and TbB_4 in the absence of SOC. Due to the collinear magnetism in TmB_4 , the spin-up (red) and spin-down (blue) Fermi surfaces are distinctly separated.

III. TbB_4 : SPIN TEXTURE IN THE ABSENCE OF SOC

SFIG. 4(a) shows the band structure of TbB_4 near the \mathbf{M} point. The bands highlighted in red are plotted as Fermi surface in SFIG. 4(b), which displays the spin-projected Fermi surfaces at the $k_z = -0.04, 0$, and 0.04 planes (in units of $2\pi/c$). Due to the symmetry elements $\{C_{2x}||M_y|\tau_{(a/2+b/2)}\}$ and $\{C_{2y}||M_x|\tau_{(a/2+b/2)}\}$, the spin textures on the Fermi surfaces are highly symmetric. The S_x and S_y spin components of the outer Fermi surface exhibit f -wave-like characteristics, while the inner Fermi surface displays a p -wave-like pattern. Furthermore, the S_z spin component shows a conventional d -wave altermagnetic spin texture.

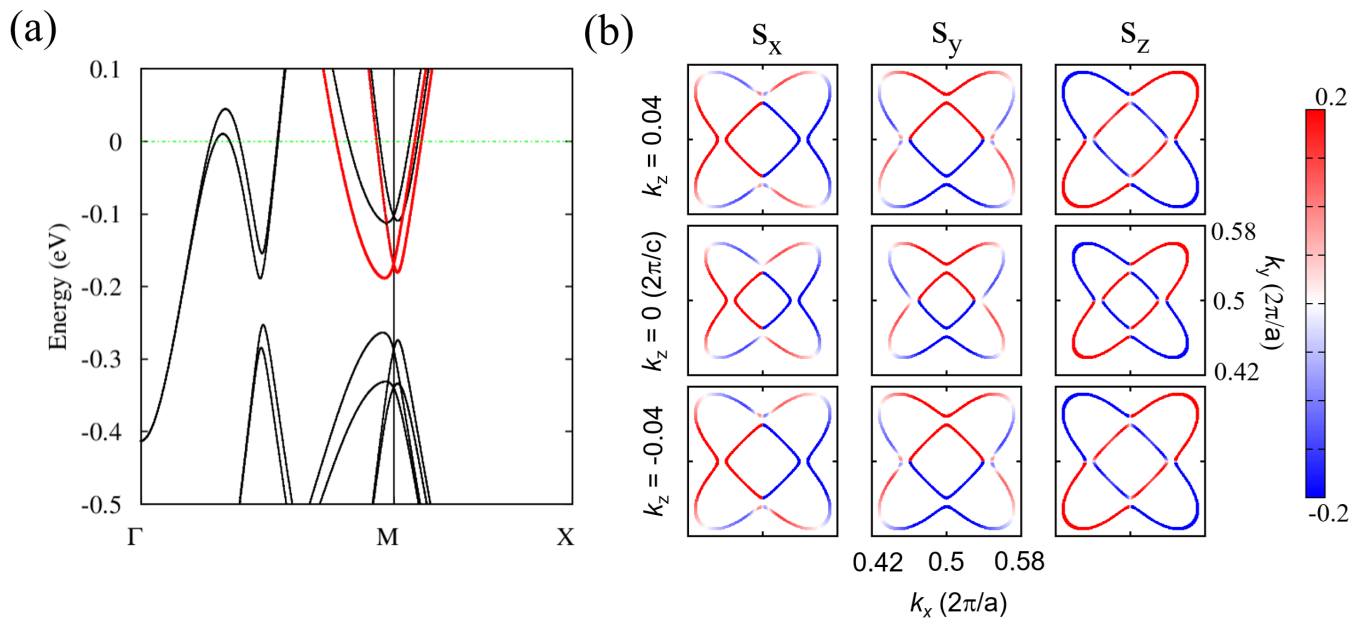


FIG. 4. (Color Online) Electronic structure of TbB_4 in the absence of SOC. (a) Bulk band structure near the M point. The spin-projected Fermi surfaces corresponding to the bands highlighted in red are shown in (b). (b) Fermi surfaces for the red bands in (a), plotted in the $k_z = -0.04, 0$, and 0.04 planes (in units of $2\pi/c$) around the M point, colored by the spin components s_x, s_y , and s_z .

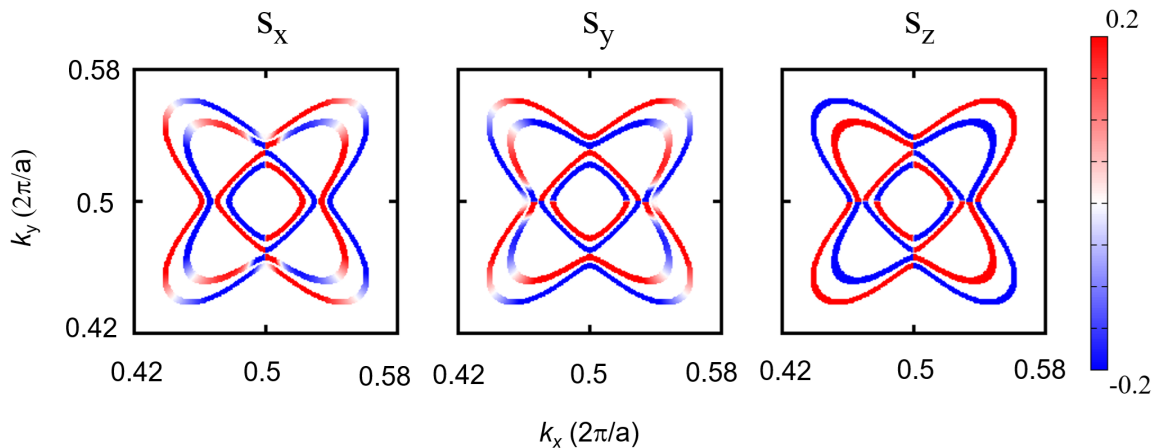


FIG. 5. (Color Online) Full Fermi surfaces corresponding to FIG. 4(a) around the M point in the $k_z = 0$ plane, colored by the spin components s_x, s_y , and s_z .

In the following section, we develop tight-binding and $\mathbf{k} \cdot \mathbf{p}$ models to elucidate the coexistence of the inner p -wave and outer f -wave spin textures for the in-plane spin components, alongside the d -wave spin texture of the S_z component.

IV. TIGHT-BINDING MODEL FOR THE NON-COPLANAR MAGNETIC STATE OF TbB_4

To understand the unique spin texture of the Fermi surface in TbB_4 , we construct a tight-binding (TB) Hamiltonian based on the Shastry-Sutherland lattice (SSL) geometry. Assuming a single orbital per sublattice and considering the two spin degree of freedom ($\sigma \in \{\uparrow, \downarrow\}$), the system is described by an 8×8 Hamiltonian matrix.

This Hamiltonian is expressed in the basis of the four SSL sublattices ($i = 1, 2, 3, 4$):

$$\Psi_{\mathbf{k}}^\dagger = \left(c_{1\uparrow}^\dagger, c_{2\uparrow}^\dagger, c_{3\uparrow}^\dagger, c_{4\uparrow}^\dagger, c_{1\downarrow}^\dagger, c_{2\downarrow}^\dagger, c_{3\downarrow}^\dagger, c_{4\downarrow}^\dagger \right)$$

where $c_{i\sigma}^\dagger$ creates an electron with spin σ at site i .

The total Hamiltonian can be expressed as

$$H = \sum_{\mathbf{k}} \Psi_{\mathbf{k}}^\dagger \mathcal{H}(\mathbf{k}) \Psi_{\mathbf{k}},$$

with

$$\mathcal{H}(\mathbf{k}) = \mathcal{H}_{kin}(\mathbf{k}) + \mathcal{H}_B(\mathbf{k}) + \mathcal{H}_{ex}$$

Here, $\mathcal{H}_{kin}(\mathbf{k})$ represents the standard electron hopping, while $\mathcal{H}_B(\mathbf{k})$ captures the complex hopping intimately tied to the non-coplanar magnetic ordering. This non-coplanar spin configuration inherently possesses a non-zero scalar spin chirality, $\mathbf{S}_i \cdot (\mathbf{S}_j \times \mathbf{S}_k) \neq 0$, which acts as an emergent pseudo-magnetic field (or Berry phase) for the itinerant electrons. Finally, \mathcal{H}_{ex} denotes the exchange interaction between the conduction electrons and the localized non-coplanar spin moments of the Tb ions.

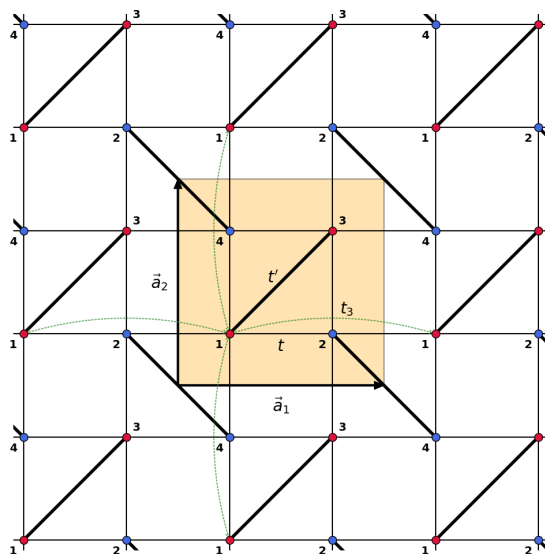


FIG. 6. (Color Online) Schematic representation of the Shastry-Sutherland lattice and the tight-binding hopping parameters. The orange-shaded area indicates the unit-cell, and the black arrows represent the Bravais lattice vectors $\vec{a}_1 = (a, 0)$ and $\vec{a}_2 = (0, a)$, where a is the lattice constant. The four sublattices are numbered 1 to 4. The thin solid lines denote the nearest-neighbor hopping (t) forming the square lattice, the thick solid lines indicate the dimer hopping (t'), and the dotted curves illustrate the next-nearest-neighbor hopping (t_3) connecting identical sublattices across adjacent unit cells. For visual clarity, t_3 is only shown for sublattice 1.

1. Standard Kinetic Hamiltonian $\mathcal{H}_{kin}(\mathbf{k})$

The 8×8 standard kinetic Hamiltonian is given by:

$$\mathcal{H}_{kin}(\mathbf{k}) = h_{kin}(\mathbf{k}) \otimes \sigma_0$$

where $h_{kin}(\mathbf{k})$ is the 4×4 spin-independent kinetic matrix and σ_0 is the 2×2 identity matrix.

To accurately capture the energy band dispersion and the topological crossing features near the Fermi level—particularly around the M-point— $h_{kin}(\mathbf{k})$ incorporates hopping pathways up to the next-nearest neighbors. As shown in SFIG. 6,

these include the nearest-neighbor hopping t on the square lattice, the intra/inter-cell diagonal dimer hopping t' , and the next-nearest-neighbor hopping t_3 connecting adjacent unit cells.

The matrix elements of h_{kin} are given by:

$$h_{\text{kin}}(\mathbf{k}) = \begin{pmatrix} \epsilon(\mathbf{k}) & t(1 + e^{-ik_x a}) & t' & t(1 + e^{-ik_y a}) \\ t(1 + e^{ik_x a}) & \epsilon(\mathbf{k}) & t(1 + e^{-ik_y a}) & t'e^{i(k_x - k_y)a} \\ t' & t(1 + e^{ik_y a}) & \epsilon(\mathbf{k}) & t(1 + e^{ik_x a}) \\ t(1 + e^{ik_y a}) & t'e^{-i(k_x - k_y)a} & t(1 + e^{-ik_x a}) & \epsilon(\mathbf{k}) \end{pmatrix}$$

where $\epsilon(\mathbf{k}) = E_0 + 2t_3(\cos(k_x a) + \cos(k_y a))$. Here, E_0 is the on-site energy for the single orbital at each sublattice, and a is the lattice constant.

2. Complex Kinetic Hamiltonian $\mathcal{H}_B(\mathbf{k})$

Even in the absence of spin-orbit coupling (SOC), the non-coplanar magnetic ordering of the Tb ions yields a non-zero scalar spin chirality, $\mathbf{S}_i \cdot (\mathbf{S}_j \times \mathbf{S}_k) \neq 0$. For itinerant electrons, this chiral spin texture acts as an emergent fictitious gauge field (Berry phase). Due to the specific non-coplanar magnetic structure of TbB₄, this gauge field is spatially *staggered* between adjacent sub-plaquettes.

To capture this staggered effective magnetic field while preserving the underlying point-group symmetries governing the spin texture, we introduce a complex hopping amplitude λ .

The 8×8 complex kinetic Hamiltonian is written as:

$$\mathcal{H}_B(\mathbf{k}) = h_B(\mathbf{k}) \otimes \sigma_0$$

where the 4×4 spin-independent complex kinetic matrix $h_B(\mathbf{k})$ is given by:

$$h_B(\mathbf{k}) = \begin{pmatrix} 0 & i\lambda(1 - e^{-ik_x a}) & 0 & i\lambda(1 - e^{-ik_y a}) \\ -i\lambda(1 - e^{ik_x a}) & 0 & i\lambda(1 - e^{-ik_y a}) & 0 \\ 0 & -i\lambda(1 - e^{ik_y a}) & 0 & i\lambda(1 - e^{-ik_x a}) \\ -i\lambda(1 - e^{ik_y a}) & 0 & -i\lambda(1 - e^{ik_x a}) & 0 \end{pmatrix}$$

Note that considering only the nearest-neighbor complex hopping is sufficient to accurately reproduce the unique Fermi surface spin texture of TbB₄.

Therefore, the total spin-independent kinetic matrix, combining both standard and complex hopping terms, becomes:

$$h_{\text{kin}}(\mathbf{k}) + h_B(\mathbf{k}) = \begin{pmatrix} \epsilon(\mathbf{k}) & t_x^+(\mathbf{k}) & t' & t_y^+(\mathbf{k}) \\ (t_x^+(\mathbf{k}))^* & \epsilon(\mathbf{k}) & t_y^+(\mathbf{k}) & t'e^{i(k_x - k_y)a} \\ t' & (t_y^+(\mathbf{k}))^* & \epsilon(\mathbf{k}) & t_x^-(\mathbf{k}) \\ (t_y^+(\mathbf{k}))^* & t'e^{-i(k_x - k_y)a} & (t_x^-(\mathbf{k}))^* & \epsilon(\mathbf{k}) \end{pmatrix} \quad (1)$$

where the complex staggered hopping elements are explicitly defined as:

$$\begin{aligned} t_x^+(\mathbf{k}) &= t(1 + e^{-ik_x a}) + i\lambda(1 - e^{-ik_x a}) \\ t_x^-(\mathbf{k}) &= t(1 + e^{ik_x a}) + i\lambda(1 - e^{-ik_x a}) \\ t_y^+(\mathbf{k}) &= t(1 + e^{-ik_y a}) + i\lambda(1 - e^{-ik_y a}) \end{aligned} \quad (2)$$

3. Exchange Interaction \mathcal{H}_{ex}

The conduction electrons interact with the localized, non-coplanar magnetic moments of the Tb ions via the $s - f$ exchange coupling. The interaction Hamiltonian at site i is $-J_{sf}\mathbf{s}_i \cdot \mathbf{S}_i$, where \mathbf{s}_i is the conduction electron spin operator (represented by Pauli matrices) and \mathbf{S}_i is the normalized local spin moment of the Tb ion.

The exchange interaction Hamiltonian \mathcal{H}_{ex} can be expressed as

$$\mathcal{H}_{\text{ex}} = \begin{pmatrix} -J_{sf}\Sigma_z & -J_{sf}\Sigma_- \\ -J_{sf}\Sigma_+ & J_{sf}\Sigma_z \end{pmatrix}$$

where Σ_z and Σ_{\pm} are 4×4 matrices representing the diagonal Zeeman-like splitting and the off-diagonal spin-mixing, respectively:

$$\Sigma_z = \begin{pmatrix} S_{1z} & 0 & 0 & 0 \\ 0 & S_{2z} & 0 & 0 \\ 0 & 0 & S_{3z} & 0 \\ 0 & 0 & 0 & S_{4z} \end{pmatrix}$$

$$\Sigma_- = \begin{pmatrix} S_{1x} - iS_{1y} & 0 & 0 & 0 \\ 0 & S_{2x} - iS_{2y} & 0 & 0 \\ 0 & 0 & S_{3x} - iS_{3y} & 0 \\ 0 & 0 & 0 & S_{4x} - iS_{4y} \end{pmatrix}$$

$$\Sigma_+ = (\Sigma_-)^\dagger.$$

These off-diagonal Σ_{\pm} matrices are directly responsible for the characteristic momentum-dependent spin texture observed on the Fermi surface, despite the absence of intrinsic spin-orbit coupling.

Consequently, by combining the kinetic and exchange terms, the total Hamiltonian $\mathcal{H}(\mathbf{k})$ takes the explicit form:

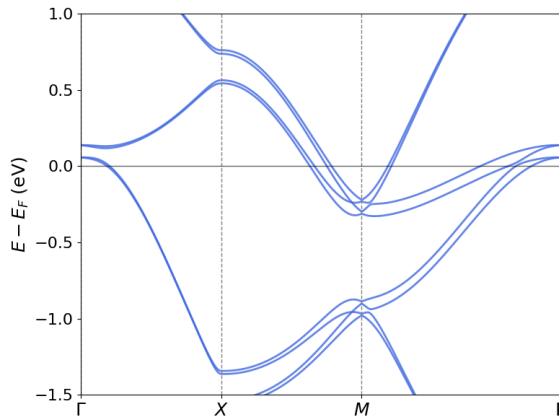
$$\mathcal{H}(\mathbf{k}) = \begin{pmatrix} h_{\text{kin}}(\mathbf{k}) + h_B(\mathbf{k}) - J_{sf}\Sigma_z & -J_{sf}\Sigma_- \\ -J_{sf}\Sigma_+ & h_{\text{kin}}(\mathbf{k}) + h_B(\mathbf{k}) + J_{sf}\Sigma_z \end{pmatrix}$$

4. Model Parameters

The tight-binding parameters used to reproduce the key features of the DFT calculations (e.g., the crossing at the M-point and the spin texture on the Fermi surface) are:

- $E_0 = -0.4$ eV (On-site energy)
- $t = -0.5$ eV (Nearest-neighbor hopping)
- $t' = -0.3$ eV (Dimer hopping)
- $t_3 = 0.05$ eV (Next-nearest-neighbor hopping)
- $J_{sf} = -0.15$ eV ($s - f$ exchange coupling)
- $\lambda = 0.01$ eV (Complex hopping)

The resulting TB band dispersion and the 2D Fermi surface displaying each spin component are presented in SFIG. 7 and SFIG. 8, respectively.



SFIG. 7. (Color Online) Tight-binding band dispersion of TbB₄. The model qualitatively captures the DFT band dispersion near the Fermi level, particularly around the M point.

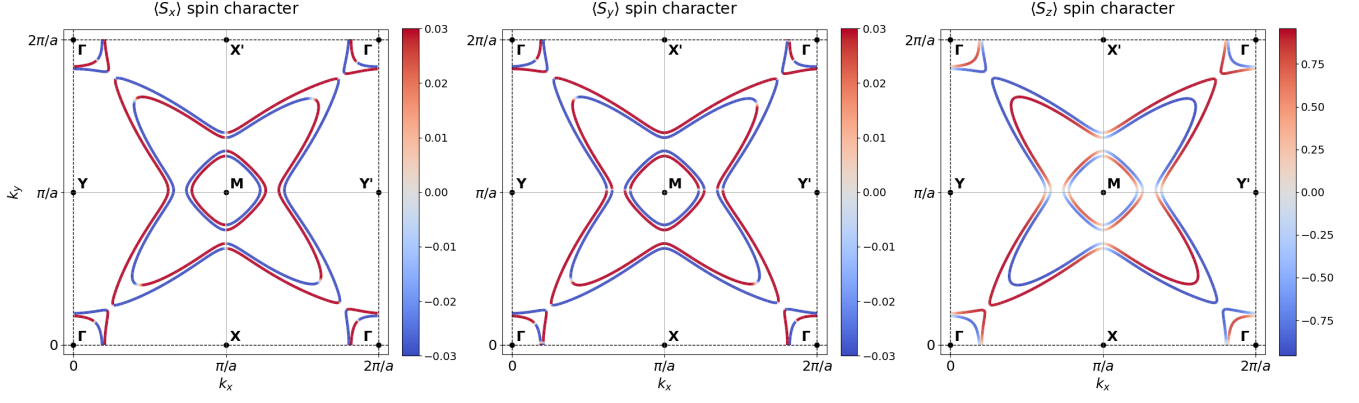


FIG. 8. (Color Online) 2D Fermi surface and its spin components obtained from the tight-binding model. The color map indicates the magnitude of the spin polarization. The model successfully reproduces the key DFT features around the M point, explicitly demonstrating the coexistence of f -wave-like and p -wave-like spin textures.

V. ANALYTICAL $\mathbf{k} \cdot \mathbf{p}$ EXPANSION AND THE ORIGIN OF MOMENTUM-DEPENDENT SPIN TEXTURES

To demonstrate how the staggered Berry phase (λ) naturally yields the coexistence of p -wave-like, d -wave-like, and f -wave-like spin textures on the 2D Fermi surface, we perform an analytical $\mathbf{k} \cdot \mathbf{p}$ expansion of the 8×8 tight-binding Hamiltonian around the M -point, $\mathbf{M} = (\pi/a, \pi/a)$.

1. TAYLOR EXPANSION OF THE KINETIC MATRIX AT THE M-POINT

We define the momentum near the M -point as $\mathbf{k} = \mathbf{M} + \mathbf{q} = (\pi/a + q_x, \pi/a + q_y)$, where $|\mathbf{q}| \ll 1$. We expand the elements of the total kinetic Hamiltonian in Eq. (1) up to the cubic order, $\mathcal{O}(q^3)$, to capture the dominant symmetries.

1.1 Nearest-Neighbor Hopping (t) and Staggered Berry Phase (λ)

Substituting $k_x = \pi/a + q_x$ into the complex staggered hopping elements in Eq. (2), we expand the phase factors $e^{-i(\pi+q_x a)} = -e^{-iq_x a}$:

$$\begin{aligned} 1 + e^{-i(\pi+q_x a)} &\approx iq_x a + \frac{1}{2}(q_x a)^2 - \frac{i}{6}(q_x a)^3 \\ 1 - e^{-i(\pi+q_x a)} &\approx 2 - iq_x a - \frac{1}{2}(q_x a)^2 + \frac{i}{6}(q_x a)^3 \end{aligned}$$

Similarly, the expansion of the phase factors $e^{-i(\pi+q_y a)}$ is:

$$1 + e^{-i(\pi+q_y a)} \approx iq_y a + \frac{1}{2}(q_y a)^2 - \frac{i}{6}(q_y a)^3$$

Using these relations, the staggered hopping elements t_x^+ , t_x^- , and t_y^+ can be analytically expanded as:

$$\begin{aligned}
t_x^+(\mathbf{M} + \mathbf{q}) &= t(1 + e^{-i(\pi+q_x a)}) + i\lambda(1 - e^{-i(\pi+q_x a)}) \\
&\approx 2i\lambda + (\lambda + it)q_x a + \frac{1}{2}(t - i\lambda)(q_x a)^2 - \frac{1}{6}(\lambda + it)(q_x a)^3 \\
t_x^-(\mathbf{M} + \mathbf{q}) &= t(1 + e^{i(\pi+q_x a)}) + i\lambda(1 - e^{i(\pi+q_x a)}) \\
&\approx 2i\lambda + (\lambda - it)q_x a + \frac{1}{2}(t - i\lambda)(q_x a)^2 - \frac{1}{6}(\lambda - it)(q_x a)^3 \\
t_y^+(\mathbf{M} + \mathbf{q}) &= t(1 + e^{-i(\pi+q_y a)}) + i\lambda(1 - e^{-i(\pi+q_y a)}) \\
&\approx 2i\lambda + (\lambda + it)q_y a + \frac{1}{2}(t - i\lambda)(q_y a)^2 - \frac{1}{6}(\lambda + it)(q_y a)^3
\end{aligned}$$

The real parts of the linear coefficients, $\lambda q_x a$ and $\lambda q_y a$, survive symmetrically, opening the pathway for the p -wave texture in the $\langle S_x \rangle$ and $\langle S_y \rangle$ components, respectively.

1.2 Dimer Hopping (t')

The inter-cell dimer hopping introduces diagonal phase factors $e^{\pm i(k_x - k_y)a}$. Near the M-point, the phase difference remains $k_x - k_y = q_x - q_y$. The Taylor expansion of this diagonal term up to the cubic order explicitly generates essential cross-terms:

$$\begin{aligned}
t' e^{i(k_x - k_y)a} &= t' e^{i(q_x - q_y)a} \\
&\approx t' \left[1 + i(q_x - q_y)a - \frac{1}{2}(q_x - q_y)^2 a^2 - \frac{i}{6}(q_x - q_y)^3 a^3 \right] \\
&= t' \left[1 + i(q_x - q_y)a - \frac{1}{2}(q_x^2 - 2q_x q_y + q_y^2)a^2 - \frac{i}{6}(q_x^3 - 3q_x^2 q_y + 3q_x q_y^2 - q_y^3)a^3 \right]
\end{aligned}$$

This rigorous expansion explicitly reveals the microscopic origin of the mixed cubic momentum terms (e.g., $3q_x q_y^2$).

1.3 Next-Nearest-Neighbor Hopping (t_3)

The diagonal on-site energy term involves t_3 and is expanded using $\cos(\pi + q_x a) = -\cos(q_x a)$:

$$\begin{aligned}
\epsilon(\mathbf{M} + \mathbf{q}) &= E_0 + 2t_3(\cos(\pi + q_x a) + \cos(\pi + q_y a)) \\
&\approx (E_0 - 4t_3) + t_3 [(q_x a)^2 + (q_y a)^2] + \mathcal{O}(q^4)
\end{aligned}$$

The t_3 hopping primarily modulates the effective band mass at $\mathcal{O}(q^2)$. This quadratic modulation critically influences the energy denominators during the downfolding perturbation theory, thereby scaling the magnitude of the resulting effective spin fields.

2. LÖWDIN DOWNFOLDING AND THE EFFECTIVE SPIN HAMILTONIAN

To extract the effective physics at the Fermi level, we project the 8×8 Hamiltonian $\mathcal{H}(\mathbf{M} + \mathbf{q})$ onto the low-energy degenerate subspace utilizing Löwdin partitioning.

The resulting 2×2 effective Hamiltonian for the conduction electrons in the pseudo-spin subspace takes the generic form:

$$\mathcal{H}_{eff}(\mathbf{q}) = \varepsilon_0(\mathbf{q})\sigma_0 + \mathbf{h}(\mathbf{q}) \cdot \boldsymbol{\sigma}$$

where σ_0 is the 2×2 identity matrix, $\boldsymbol{\sigma} = (\sigma_x, \sigma_y, \sigma_z)$ are the Pauli matrices, and $\mathbf{h}(\mathbf{q})$ is the momentum-dependent effective Zeeman field.

3. COEXISTENCE OF p -WAVE, d -WAVE, AND f -WAVE SPIN SYMMETRIES

3.1 The Inner Pocket (In-Plane): p -wave Symmetry

During downfolding, the pure real-hopping linear terms ($\pm itq_x a$ and $\pm itq_y a$) destructively interfere and cancel out due to the staggered $s - f$ exchange potential. However, the staggered Berry phase ($\lambda \neq 0$) breaks this cancellation. The symmetric real parts ($\lambda q_x a$ and $\lambda q_y a$) constructively survive, yielding the leading-order effective in-plane spin field:

$$\mathbf{h}_{\parallel}^{(1)}(\mathbf{q}) = \alpha \lambda J_{sf} a (q_x \hat{x} \pm q_y \hat{y})$$

This purely linear momentum dependence dictates the p -wave spin texture of the inner Fermi surface pocket around the M-point.

3.2 The Outer Pocket (In-Plane): f -wave Symmetry & Spin-Space Group Connection

As $|\mathbf{q}|$ increases, higher-order kinetic terms dominate. Through the Löwdin partitioning, combinations of the microscopic hopping pathways (t, t', t_3) yield the generalized phenomenological form dictated by the macroscopic Spin-Space Group (SSG) symmetries:

$$\mathbf{h}_{\parallel}^{(3)}(\mathbf{q}) = J_{sf} a^3 [c_1 (q_x^3 \hat{x} \pm q_y^3 \hat{y}) + c_2 (q_x q_y^2 \hat{x} \pm q_x^2 q_y \hat{y})]$$

Here, c_1 and c_2 are constant coefficients. The pure orthogonal hopping (t) contributes solely to the isolated cubic terms (q_x^3), whereas the diagonal dimer hopping (t') contributes to both the isolated and the mixed cross-terms ($(q_x \pm q_y)^3$). Consequently, the coefficients obey the strict proportionalities:

$$\begin{aligned} c_1 &\approx \mathcal{A}t + \mathcal{B}t' \\ c_2 &\approx 3\mathcal{B}t' \end{aligned}$$

where the prefactors \mathcal{A} and \mathcal{B} emerge from the third-order Löwdin perturbation expansion. Specifically, they are inversely proportional to the square of the characteristic energy gap, Δ_M , which separates the low-energy effective subspace from the high-energy bands at the M-point. This energy denominator is explicitly determined by the diagonal energy and the dimer splitting evaluated at $\mathbf{q} = 0$:

$$\Delta_M \approx |\epsilon(\mathbf{M}) \pm t'| = |(E_0 - 4t_3) \pm t'|$$

Therefore, the proportionality factors functionally scale as:

$$\mathcal{A}, \mathcal{B} \propto \frac{1}{\Delta_M^2} = \frac{1}{((E_0 - 4t_3) \pm t')^2}$$

This explicit relationship provides a profound physical insight: the fundamental presence of the mixed cubic harmonics ($c_2 \neq 0$) required by SSG theory is microscopically driven by the diagonal dimer hopping (t'). This demonstrates that the tight-binding model perfectly captures the generalized f -wave spin texture of the outer Fermi surface pocket.

3.3 The Out-of-Plane Component (S_z): d -wave Symmetry

Macroscopic symmetries strictly forbid odd-parity terms (linear q and cubic q^3) for the out-of-plane effective field $h_z(\mathbf{q})$. Consequently, the lowest non-vanishing term emerges strictly at the quadratic order ($\mathcal{O}(q^2)$):

$$h_z^{(2)}(\mathbf{q}) = \gamma J_{sf} a^2 q_x q_y$$

This purely quadratic momentum dependence generates a quadrupole-like phase winding, rigorously explaining the d -wave symmetry observed in the S_z component across the entire Fermi surface.

In summary, the phenomenological $\mathbf{k} \cdot \mathbf{p}$ model explicitly confirms that the coexistence of the inner p -wave and outer f -wave spin textures on the 2D Fermi surface is not a consequence of external spin-orbit coupling, but a rigorous

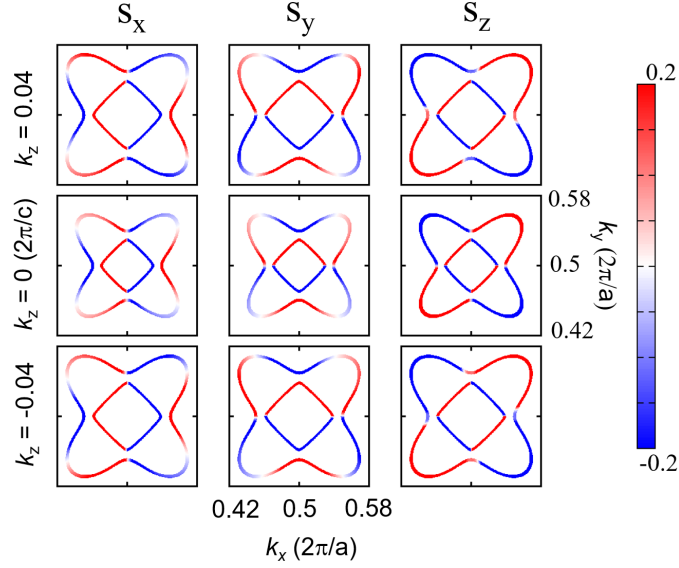


FIG. 9. (Color Online) Spin textures on the Fermi surfaces of TbB_4 in the presence of SOC, on the $k_z = -0.04, 0,$ and 0.04 planes (in units of $2\pi/c$) around the M point. Because the symmetry constraints imposed by $\{C_{2x}||M_y|\tau_{(a/2+b/2)}\}$, $\{C_{2y}||M_x|\tau_{(a/2+b/2)}\}$, and $\{E||M_z\}$ are relaxed upon the inclusion of SOC, the resulting spin textures exhibit slight deviations.

mathematical outcome of the emergent staggered Berry phase (λ) induced by the scalar spin chirality. The gauge field λ elegantly rescues the linear momentum terms from cancellation, generating the robust p -wave inner pocket, while the inherent lattice geometry naturally provides the higher-order kinetic modulations for the f -wave outer pocket. Simultaneously, symmetry constraints strictly enforce a quadratic term for the out-of-plane direction, cleanly isolating the d -wave symmetry observed in the S_z component.

VI. SPIN TEXTURES OF TbB_4 IN THE PRESENCE OF SOC

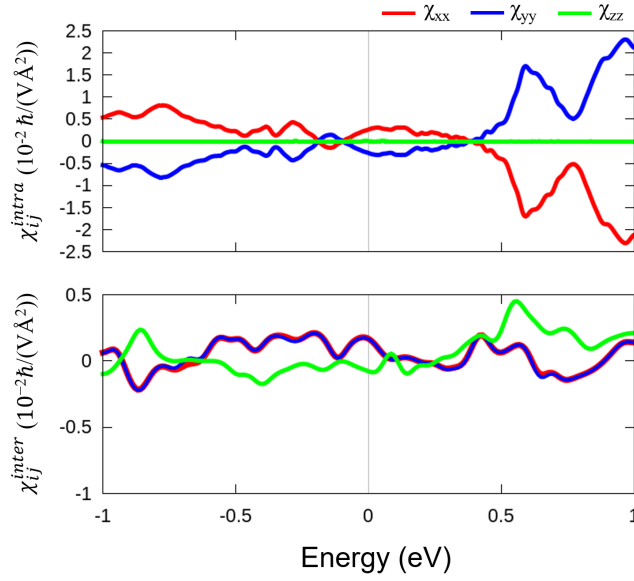
FIG. 9 shows the spin textures of TbB_4 in the presence of SOC on the $k_z = -0.04, 0,$ and 0.04 planes (in units of $2\pi/c$). Upon the inclusion of SOC, the spin-symmetry constraints imposed by $\{C_{2x}||M_y|\tau_{(a/2+b/2)}\}$, $\{C_{2y}||M_x|\tau_{(a/2+b/2)}\}$, and $\{E||M_z\}$ are relaxed. Nevertheless, the overall behavior of each spin component is largely preserved on the high-symmetry planes, which is consistent with the underlying magnetic group symmetries $C_{2x}\tau_{(a/2+b/2)}$, $C_{2y}\tau_{(a/2+b/2)}$, and C_{2z} . As a result, the spin textures retain their overall structures on high-symmetry planes (e.g., $k_z = 0$), whereas they exhibit slight deviations as one moves away from these planes.

VII. EDELSTEIN RESPONSES OF TbB_4 IN THE PRESENCE OF SOC

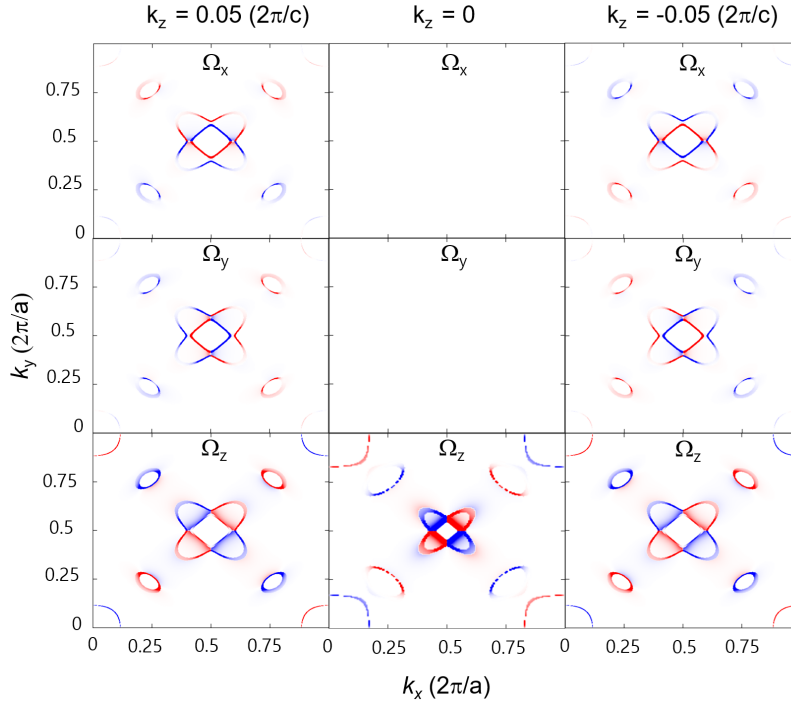
In the absence of SOC, spin group symmetries restrict the finite Edelstein response to only two components, χ_{xx} and χ_{yy} . Upon the inclusion of SOC, the $\{E||M_z\}$ symmetry is relaxed, allowing χ_{zz} to become nonzero. Nevertheless, the magnetic group symmetry $C_{4z}PT$ imposes a weak constraint that renders $\chi_{zz}^{\text{intra}} = 0$. This arises because χ^{intra} and χ^{inter} correspond to the real and imaginary parts of the correlation function, respectively, and the $C_{4z}PT$ operation involves complex conjugation. Meanwhile, the conditions $\chi_{xx}^{\text{intra}} = -\chi_{yy}^{\text{intra}}$ and $\chi_{xx}^{\text{inter}} = \chi_{yy}^{\text{inter}}$ are strictly maintained under the $C_{4z}PT$ symmetry. The calculated χ^{intra} and χ^{inter} in the presence of SOC are shown in SFIG. 10.

VIII. BERRY CURVATURE AND BERRY CURVATURE DIPOLE OF TbB_4

As discussed in the main text, without taking SOC into account, both the integral of the Berry curvature over the entire Brillouin zone (BZ) and the Berry curvature dipole (BCD) strictly vanish. This is clearly demonstrated in SFIG. 11.



SFIG. 10. (Color Online) Calculated Edelstein response tensor χ_{ij} of TbB_4 in the presence of SOC. (a) Intraband contribution χ_{ij}^{intra} and (b) interband contribution χ_{ij}^{inter} .



SFIG. 11. (Color Online) Momentum-space distribution of the Berry curvature $\Omega_i(\mathbf{k})$ for TbB_4 in the absence of SOC, evaluated on the $k_z = -0.05, 0,$ and 0.05 planes (in units of $2\pi/c$) around the M point. In the $k_z = 0$ plane, the in-plane components $\Omega_x(\mathbf{k})$ and $\Omega_y(\mathbf{k})$ strictly vanish due to the $\{E||M_z\}$ spin-group symmetry.

Although a nonzero local Berry curvature $\Omega_i(\mathbf{k})$ is allowed in TbB_4 even in the absence of SOC, the spin-group symmetry elements $\{C_{2x}||C_{2x}|\tau_{(a/2+b/2)}\}$, $\{C_{2y}||C_{2y}|\tau_{(a/2+b/2)}\}$, and $\{C_{2z}||C_{2z}\}$, dictate that its integral over the entire BZ must be zero. This feature is well demonstrated in SFIG. 11, where $\Omega_i(\mathbf{k})$ is plotted on the $k_z = -0.05, 0,$ and 0.05 planes (in units of $2\pi/c$) in the absence of SOC. Note that $\Omega_x(\mathbf{k})$ and $\Omega_y(\mathbf{k})$ strictly vanish over the $k_z = 0$ plane due to the $\{E||M_z\}$ spin-group symmetry.

Upon the inclusion of SOC, however, the BCD can become nonzero, even while the net Berry curvature remains

zero. The momentum-space distribution of $\Omega_i(\mathbf{k})$ shown in Fig. 4 of the main text clearly demonstrates that the BCD components D_{xx} and D_{yy} can be nonzero, thereby giving rise to a nonlinear Hall effect in TbB₄.



* dcrhyu@postech.ac.kr

† Co-corresponding: bongjae@knu.ac.kr

‡ Co-corresponding: cjkang87@cnu.ac.kr

- [1] Z. Heiba, W. Schäfer, E. Jansen, and G. Will, Low-temperature structural phase transitions of tbb4 and erb4 studied by high resolution x-ray diffraction and profile analysis, *Journal of Physics and Chemistry of Solids* **47**, 651 (1986).
- [2] G. Kresse and D. Joubert, From ultrasoft pseudopotentials to the projector augmented-wave method, *Phys. Rev. B* **59**, 1758 (1999).
- [3] G. Kresse and J. Furthmüller, Efficient iterative schemes for ab initio total-energy calculations using a plane-wave basis set, *Phys. Rev. B* **54**, 11169 (1996).
- [4] J. P. Perdew, K. Burke, and M. Ernzerhof, Generalized gradient approximation made simple, *Phys. Rev. Lett.* **77**, 3865 (1996).
- [5] R. D. Johnson and S. W. Lovesey, Magnetic symmetries of terbium tetraboride (Tbb₄) revealed by resonant x-ray bragg diffraction, *Phys. Rev. B* **110**, 104405 (2024).